Utrecht University

Faculty of Science, Utrecht University
Institute for Subatomic Physics

The Contribution of Event Shapes to Elliptic Flow in pp-Collisions at $\sqrt{s} = 13$ TeV at the LHC with ALICE

BACHELOR THESIS

Noor Koster

Supervisor:

Dr. PANOS CHRISTAKOGLOU
Institute for Subatomic Physics
Dutch National Institute for Subatomic Physics (NIKHEF)

June 10, 2020

Abstract

Recent discoveries of collective behaviour in proton-proton collisions at ultra-relativistic energies measured at the Large Hadron Collider (LHC) have gained great interest, since they provide new insights on the behaviour of matter at extreme temperatures and densities. The newly observed collectivity is, to a great extent, similar to observations in Pb-Pb collisions where they indicate the existence of a Quark Gluon Plasma (QGP). The QGP transforms initial eccentricities in space to elliptic anisotropies in momentum space where it is measured as elliptic flow (v_2). Elliptic flow in pp-collisions is measured around the same magnitude as in Pb-Pb collisions however, pp-collisions do not contain the elliptic overlap area that generates the spatial eccentricity in Pb-Pb collisions. This raises the question whether the observed elliptic flow in pp-collisions is generated by a QGP or can be generated by other underlying principles.

This thesis presents measurements on the contribution of event shapes to v_2 using two and multi particle cumulants in pp-collisions at $\sqrt{s} = 13\text{TeV}$. Data is obtained from measurements at the LHC with the ALICE detector and from events simulated by two tunes of the PYTHIA8 model. A technique called event shape engineering is used to separate the inclusive events and study the multiplicity dependence of elliptic flow for events having low, mid and high sphericities. The collision data shows how measurements on v_2 at low multiplicities are biased by low sphericity event shapes, most dominant in this range, and together with the consistent PYTHIA8 simulations show no QGP is required to generate v_2 at low multiplicities in inclusive pp-collisions. The results on mid and high sphericity events show how the addition of colour reconnection in the PYTHIA8 model improves the performance for all multiplicities and thereby supports the theory that colour reconnection generates collective effects.

Contents

1   Introduction

Studying high-energy collisions between nuclei in particle accelerators like the Large Hadron Collider (LHC) provides insight on the behaviour of matter at extremely high temperatures and densities. In this energy regime the theory of quantum chromodynamics (QCD) predicts a phase transition between a hadronic phase, like our present universe, and a deconfined state of matter, the quark-gluon plasma (QGP)[1].

Quantum chromodynamics provides a theoretical framework on the behaviour of quarks and their interactions with gluons described by colour charge quantum numbers, the strong force. The theory describes the unique interactions of gluons, which can couple not only to quarks but to other gluons as well. This so-called self-coupling is probably causing the force between quarks and gluons to strengthen at increasing distance and at the same time weakens the force when they get closer to each other. The former called confinement and the latter asymptotic freedom [2]. Confinement forces our present universe to exist in a bound hadronic state. This assures no gluon or quark has ever been observed independently propagating macroscopic distances through space. However, in the first few microseconds of our universe when the energy density was high enough, the theory allows for hadrons to deconfine into freely moving and highly interacting quarks and gluons, the quark-gluon plasma. The energy density at which this transition occurs is calculated to be $0.7 \pm 0.2 \text{GeV/fm}^3$, which is five times the density of nuclear matter[3].

In central Pb-Pb collisions at the LHC at a centre of mass energy $\sqrt{s_{\text{NN}}} = 2.76 \text{TeV}$, the reached energy density is about 15GeV/fm^3 [4]. This is far above the transition density and thus creates the conditions necessary to study the predicted phase transition. The lifetime of the QGP in these collisions is calculated to be about 10^{-22}s [3], making it transform back into hadronic matter before reaching any detector at the LHC. However, the particle cascade that follows should reflect some of the properties of a QGP if it was formed. One of these properties, called *anisotropic flow*, is the main subject of this thesis and will be studied in its most dominant form, *elliptic flow*. It reflects the anisotropicity of the final azimuthal momentum distribution of all particles in an event with elliptic flow only looking at elliptical deformations.
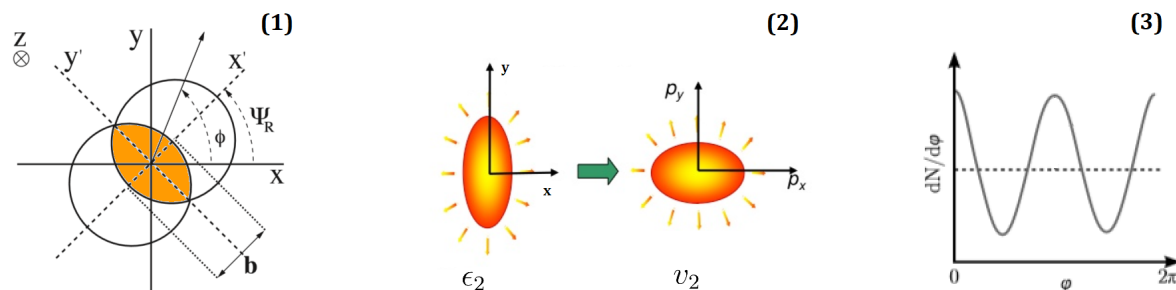
Figure 1: **(1)** The impact parameter b together with the symmetry plane angle Ψ_R and the azimuthal angle ϕ (φ) seen from the laboratory frame with the x,y-plane perpendicular to the beam axis. [5] **(2)** The translation from spatial anisotropy, characterized by the eccentricity ε_2, to the momentum space anisotropy, characterized by v_2 in the rotated '-frame [6]. **(3)** The corresponding final azimuthal particle distribution as a function of the azimuthal angle φ.

Elliptic flow originates in the overlap area between two colliding nuclei. This area is characterized by the impact parameter b, which not only defines the distance between the centres of the nuclei but also the direction of the symmetry plane, visualised in figure 1.1. The overlap region ranges from almost isotropic head-on collisions to highly elliptical in peripheral collisions. The droplet of QGP created in the collision contains the shape of the initial overlap zone and can therefore be highly anisotropic, this spatial ellipticity is characterised by the eccentricity ε_2, see figure 1.2. During the hydrodynamic expansion of these elliptical droplets, the pressure gradients increase towards a maximum at the short axis, resulting in an elliptic anisotropy in momentum space, characterized by elliptic flow v_2. The momentum anisotropy affects all particles and results in an anisotropic correlated particle distribution, see figure 1.3, with more particles flying in-plane (x-direction) than out-plane (y-direction) which can be detected and studied with high statistical accuracy.

The translation from ε_2 to v_2 is proportional to first order and highly dependent on the viscosity of the medium. Comparison between experimental data and viscous hydrodynamic models required a small value for the viscosity around roughly $\eta/s \geq 1/4\pi$, making the QGP the most ideal liquid ever observed [7]. During these observations proton-proton collisions were used to provide baseline measurements, since it was assumed no QGP was created here. However, the increasing centre of mass energies at the LHC produced events with multiplicities comparable to peripheral heavy-ion collisions and led to some unexpected results.

Measurements on the two particle correlations in high multiplicity ($N_{ch} > 105$) pp events at a centre of mass energy $\sqrt{s} = 13\text{TeV}$ resulted in the same ridge like structure in the azimuthal particle distribution as Pb-Pb collisions where they are a signature of the QGP [8]. Estimating v_2 from these two particle correlations in pp-collisions leads to finite magnitudes of the same order as found in Pb-Pb collisions at $\sqrt{s} = 5.02\text{TeV}$. Figure 3 shows the multiplicity dependence of v_2 determined from two particle correlations for both pp and Pb-Pb collisions together with two other collision systems. As can be seen from the figure, the Pb-Pb data where flow is dominant is properly described by the hydrodynamic models, especcially for $N_{ch} > 300$. The trend and magnitude of the pp data is in sharp contrast with the multiplicity dependence of the hydrodynamic model but can also not be explained completely by the PYTHIA8 model, which does not contain any collective effects [9]. These observations raised the question whether the collective effects observed in pp-collisions have the same origin as in heavy-ion collisions or result from other underlying principles.

In contrast to elliptic flow generated by the eccentricity of the overlap zone between two nuclei in heavy ion collisions, elliptic flow in pp-collisions does not have this spatial analogue that generates the momentum space anisotropy. However, due to energy and momentum conservation from hard scatterings between quarks and gluons, more dominant in small systems, the final azimuthal particle distributions in pp-collisions exhibit the same kind of final state anisotropies as Pb-Pb collisions. Consisiting of mainly back-to-back jet structured momentum conserving events for low multiplicities and increasing in anisotropy for higher multiplicities. This means the event shape could bias the measured flow coefficients, with the most dominant contribution at low multiplicity, and generate collective like effects.
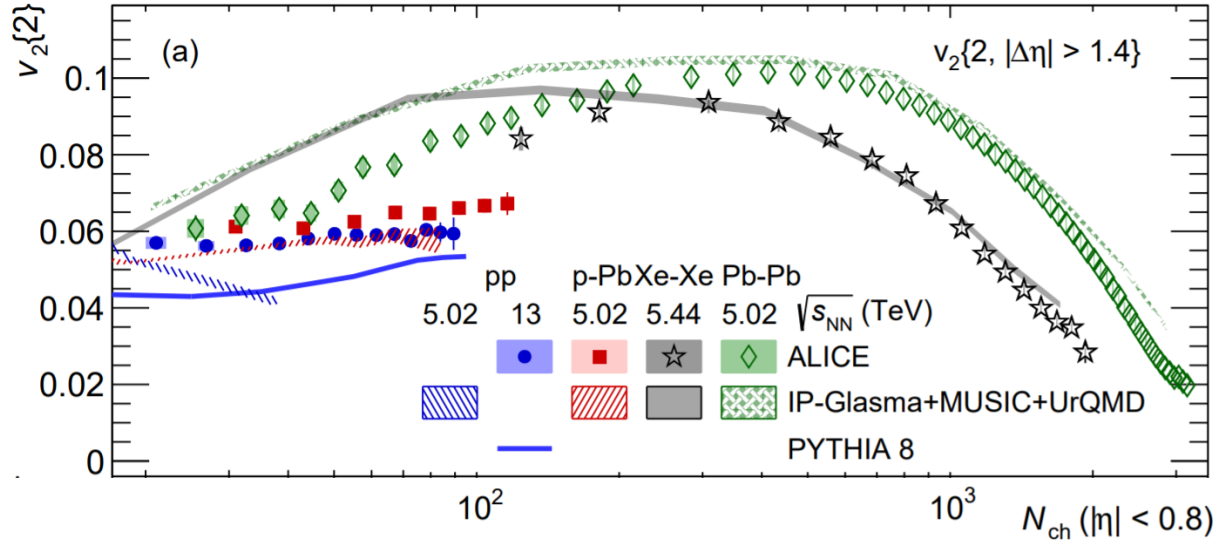
Figure 2: Multiplicity dependence of $v_2\{2\}$ (v_2 calculated from two particle correlations) for Pb-Pb, *Xe-Xe*, *p-Pb* and pp-collisions. The data is compared with the hydrodynamic IP-Glasma+MUSIC+UrQMD model and the pp data for $\sqrt{s} = 13$Tev is compared to the PYTHIA8 model. Figure adapted from Ref. [9]

This assumption gives rise to the main question sought to be answered in this thesis: *Can event shapes in* pp *collisions bias the* v_2 *measurements and induce collective flow-like effects?*

Events in pp-collisions can be disentangled by selection on their final state event shape in the transverse plane, measured as transverse sphericity. This observable can separate the isotropic particle distributions from the back-to-back events. This technique is called event shape engineering and is used in this thesis to study the contribution of different event shapes to v_2. The results obtained with this technique are visualized alongside two tunes of the PYTHIA8 model, containing only hard scattering effects, to determine if the measured v_2 values can indeed be reproduced without the formation of a QGP.

The remaining of this thesis is organized as follows. In Chapter 2 the method used to determine v_2 is summarised in detail, followed by a description of the transverse sphericity. The analysis details are summarized in Chapter 3 together with a description of the PYTHIA8 model tunes. The results from the analysis will be presented and discussed in Chapter 4 and lead to the conclusions summarized in Chapter 5 together with suggestions for further research.

2 Anisotropic Flow and Event Shape Engineering

2.1 Flow Coefficients

Anisotropic flow is reflected in the final azimuthal particle distribution and defined in its Fourier expansion[10],

$$\frac{dN}{d\varphi} \propto 1 + 2 \sum_{n=1}^{\infty} v_n \cos[n(\varphi - \Psi_n)], \tag{1}$$

with v_n the flow coefficient, Ψ_n the symmetry plane angle of the nth harmonic and φ the azimuthal angle of produced particles. The flow coefficients are given by,

$$v_n = \langle \cos(n(\varphi - \Psi_n)) \rangle, \tag{2}$$

where $\langle \ldots \rangle$ denotes the average taken over all particles, summed over all events. In general, when v_n is a function of both rapidity and transverse momentum it is called differential flow. In this thesis v_n will be averaged over the phase-space region covered by the detector's acceptance and in this form it is called integrated flow. Different coefficients are associated with different types of anisotropies, v_1 indicates directed, v_2 elliptic, v_3 triangular and v_4 squared anisotropies, illustrated in figure 3.
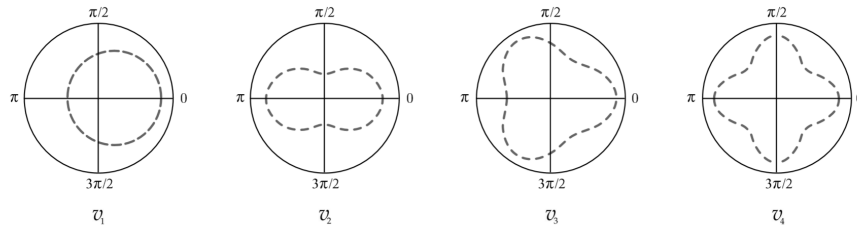

Figure 3: A visualisation of the first four flow coefficients in the transverse plane[11].

The flow coefficients can be determined from equation 2 if both Ψ_n and the event by event azimuthal particle distributions are known. The azimuthal particle distribution can be determined experimentally with particle detectors while the symmetry plane angle Ψ_n cannot. The only way to determine v_n is by estimations from the azimuthal correlations between particles. Since correlations between every particle and a common symmetry plane should generate correlations among all particles.

As mentioned in the introduction, this thesis will focus only on elliptic flow so both equation 1 and 2 will be considered only in the case $n = 2$.

2.1.1 Azimuthal Correlations

The azimuthal correlations are defined by,

$$\langle\langle 2\rangle\rangle \equiv \left\langle\left\langle e^{i2(\varphi_1-\varphi_2)}\right\rangle\right\rangle,$$
$$\langle\langle 4\rangle\rangle = \left\langle\left\langle e^{i2(\varphi_1+\varphi_2-\varphi_3-\varphi_4)}\right\rangle\right\rangle,$$
$$\langle\langle 6\rangle\rangle = \left\langle\left\langle e^{i2(\varphi_1+\varphi_2+\varphi_3-\varphi_4-\varphi_5-\varphi_6)}\right\rangle\right\rangle,$$
$$\langle\langle 8\rangle\rangle = \left\langle\left\langle e^{i2(\varphi_1+\varphi_2+\varphi_3+\varphi_4-\varphi_5-\varphi_6-\varphi_7-\varphi_8)}\right\rangle\right\rangle,$$
(3)

where $\langle\langle...\rangle\rangle$ denotes taking averages over all particles in an event, summed over all events and φ_{1-8} represent the angles of different particles.

Azimuthal correlations form the basis in estimating the flow coefficients but are not a direct replacement for Ψ_n. For example, following Ref.[12], the relation between the two-particle correlations and elliptic flow can be derived as:

$$\begin{aligned}
\langle\langle 2\rangle\rangle \equiv \left\langle\left\langle e^{i2(\varphi_1-\varphi_2)}\right\rangle\right\rangle &= \left\langle\left\langle e^{i2(\varphi_1-\Psi_2-(\varphi_2-\Psi_2))}\right\rangle\right\rangle, \\
&= \left\langle\left\langle e^{i2(\varphi_1-\Psi_2)}\right\rangle\left\langle e^{-i2(\varphi_2-\Psi_2)}\right\rangle + \delta_2\right\rangle, \\
&= \left\langle v_2^2 + \delta_2\right\rangle,
\end{aligned}$$
(4)

where δ_2 describes correlations between particles not related to Ψ_2, called non-flow.

Non-flow finds its origin in correlations between few particles like correlated decay products from the same mother or particles propagating in the same jet and back-to-back correlations due to momentum conservation [13]. If δ_2 is negligible compared to v_2^2, equation 4 can be used to determine v_2 directly from the two particle correlations[1], however in proton-proton collisions the small multiplicity allows non-flow to contribute significantly to the overall azimuthal correlations resulting in a non-vanishing δ_2 for all multi-particle correlations. A technique commonly used to reduce the contribution of non-flow in the low multiplicity regime is subtracting all lower particle correlations from a higher order correlation.
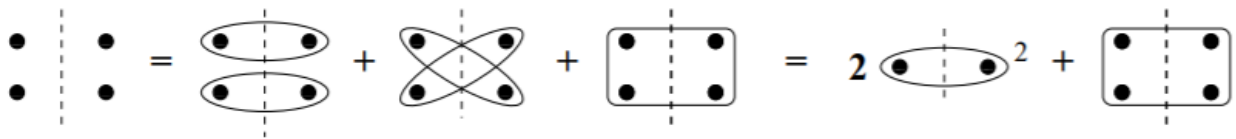

Figure 4: Decomposition of all possible correlations with four identical particles. On the right-hand side, the firs term contains the two particle correlations and the second only the correlation between all four particles together[11].

2.1.2   Multi-Particle Cumulants

The technique described above will expand the multiparticle azimuthal correlations to the so called multi-particle cumulants $c_2\{n\}$[11]. The two particle cumulant is equal to its azimuthal correlation since there are no lower orders to subtract giving

$$c_2\{2\} = \langle\langle 2\rangle\rangle.$$
(5)

---

[1]Meaning equation 4 can be simplified as $\langle\langle 2\rangle\rangle = \left\langle v_2^2 + \delta_2\right\rangle \approx \left\langle v_2^2\right\rangle$.
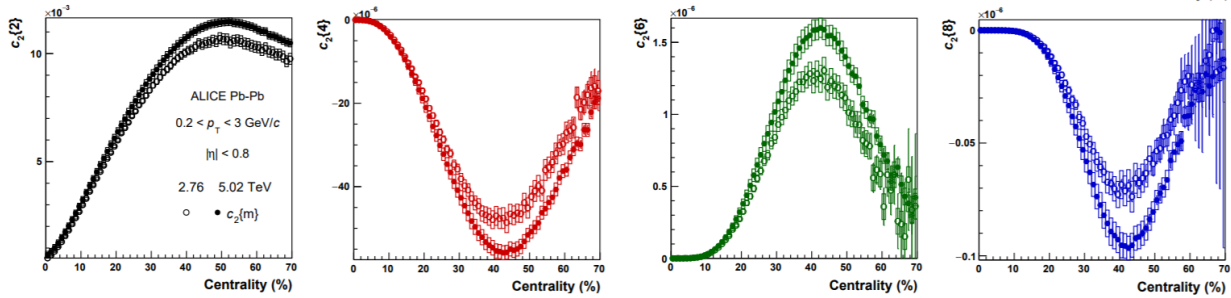
Figure 5: The centrality dependence of the cumulants in Pb-Pb collisions. Both the two and six particle cumulants have a positive sign for all centralities while the four and eight particle cumulants have a negative sign[14].

The four particle cumulant is visualized by the reordering of figure 4[2] and given by:

$$c_2\{4\} = \langle\langle 4\rangle\rangle - 2\langle\langle 2\rangle\rangle^2 \tag{6}$$

The six- and eight- particle cumulants are constructed in the same way and are given by:

$$
\begin{aligned}
c_2\{6\} &= \langle\langle 6\rangle\rangle - 9\langle\langle 4\rangle\rangle\langle\langle 2\rangle\rangle + 12\langle\langle 2\rangle\rangle^3, \\
c_2\{8\} &= \langle\langle 8\rangle\rangle - 16\langle\langle 6\rangle\rangle\langle\langle 2\rangle\rangle - 18\langle\langle 4\rangle\rangle^2 + 144\langle\langle 4\rangle\rangle\langle\langle 2\rangle\rangle^2 - 144\langle\langle 2\rangle\rangle^4.
\end{aligned}
\tag{7}
$$

These multi-particle cumulants should provide independent and accurate estimates for the same order flow coefficient v_2. They are measured as:

$$
\begin{aligned}
v_2\{2\} &= \sqrt{c_2\{2\}}, \\
v_2\{4\} &= \sqrt[4]{-c_2\{4\}}, \\
v_2\{6\} &= \sqrt[6]{\frac{1}{4}c_2\{6\}}, \\
v_2\{8\} &= \sqrt[8]{-\frac{1}{33}c_2\{8\}}.
\end{aligned}
\tag{8}
$$

These equations show that in order to get real valued estimates for v_2 the cumulants should be distributed around zero with both $c_2\{4\}$ and $c_2\{8\}$ negative and $c_2\{2\}$ and $c_2\{6\}$ positive.

As can be seen in figure 5 this specific cumulant distribution is observed in heavy-ion collisions and seen as evidence for the existence of the formation of a QGP reflecting its collective expansion. Therefore, studying the cumulant distribution in proton-proton collisions can already provide information about the origin of the observed collective effects.

2.2 Sphericity

The observable used for event shape engineering in this analysis is the transverse sphericity as a measure for the final state topology. This observable is defined by the eigenvalues of the
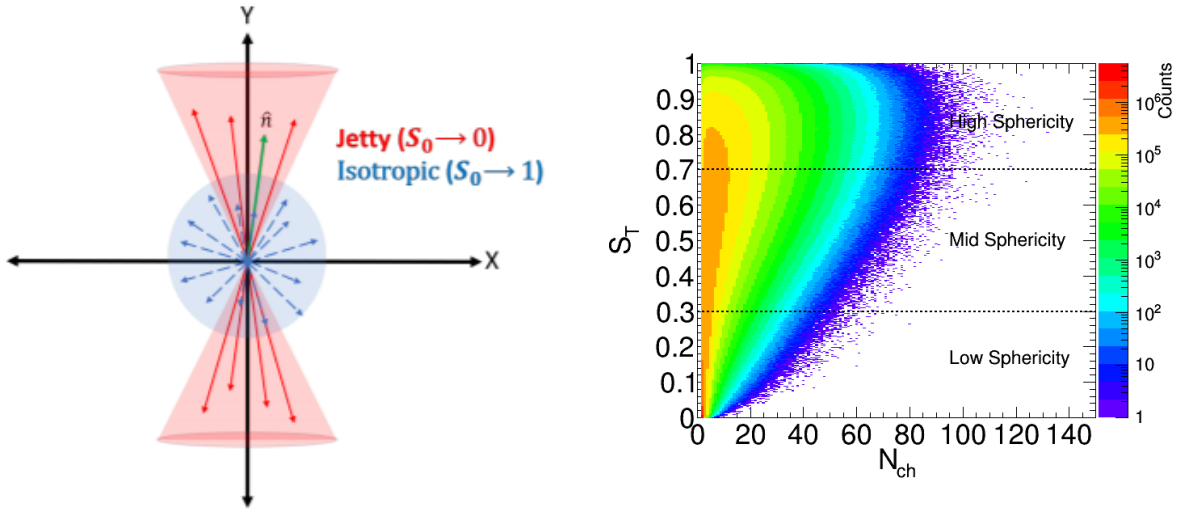
(a) Figure from Ref.[15]

(b) The distribution of events with a certain sphericity, the colours indicate the number of occurances.

Figure 6: The limits on S_T shown in (a) and the sphericity distribution in (b).

linearized transverse-momentum tensor[15]:

$$\mathbf{S^L_{xy}} = \frac{1}{\Sigma_i p_{Ti}} \sum_i \frac{1}{P_{Ti}} \begin{pmatrix} p_{xi}^2 & p_{xi}p_{yi} \\ p_{xi}p_{yi} & p_{yi}^2 \end{pmatrix}, \tag{9}$$

with the transverse sphericity defined as:

$$S_T \equiv \frac{2\lambda_2}{\lambda_1 + \lambda_2}, \tag{10}$$

where λ_1 and λ_2 are the eigenvalues of $\mathbf{S^L_{xy}}$ and obey the relation $\lambda_1 \geq \lambda_2$.

The limits of transverse sphericity are associated with two characteristic particle configurations in the transverse plane. The limit for $S_T \to 0$ specifies pencil-like events and for $S_T \to 1$ events approach an isotropic configuration, both are visualized in figure 6a.

In this thesis the analysed events will be divided according to their sphericity in three ranges. The first referred to as low sphericity will describe all events with $0 < S_T < 0.3$, mid sphericity $0.3 < S_T < 0.7$ and high sphericity $0.7 < S_T < 1.0$. Figure 6b shows the sphericity distribution of all events with 20% of all events tagged as low, 53% as mid and 28% as high sphericity events. The distribution in figure 6 shows how low sphericity events are most dominant for low multiplicities and see their numbers decrease rapidly to only a few occasional measurements for multiplicities above 60. The figure also shows the more dominant contribution of high sphericity events at increasing sphericities. The mid sphericity does not exhibit this individual dominance for any multiplicity range.

3   Analysis Details

The results for the proton-proton collisions presented in this thesis were obtained from data recorded by the ALICE detector, during LHC Run 2 data taking. Three data samples are used, recorded in 2016, 2017 and 2018 at a centre of mass energy $\sqrt{s} = 13\text{TeV}$.

3.1   ALICE

ALICE (A Large Ion Collider Experiment) is currently one of four experiments at the LHC and is optimized to study the QGP created in heavy ion (Pb-Pb) collisions. Understanding the properties of the QGP requires a solid knowledge of the underlying dynamics in these collisions. Therefore, measurements on small collision systems (proton-proton and proton-nucleus) are an essential part of ALICE as well.

The ALICE detector[16] consists of 18 different subsystems which can be divided in three categories: the central-barrel detectors, forward detectors and the muon spectrometers. Only the main properties of the subdetectors used for the analysis in this thesis will be summarized here. A complete description for all detectors can be found in Ref.[17].

The innermost detector in the central barrel is the Inner Tracking System (ITS)[18]. It consists of six cylindrical layers of silicon pixel (SPD), drift (SDD) and strip (SSD) detectors. Reconstruction of the primary collision vertex and vertices generated by the decay of primary particles or through interactions with the detector together with the identification of charged particles as its main goal. The detector has full azimuthal acceptance and a polar acceptance of $|\eta| < 2.0$[3].

(a) Inner Tracking System [19]   (b) Time Projection Chamber [20]
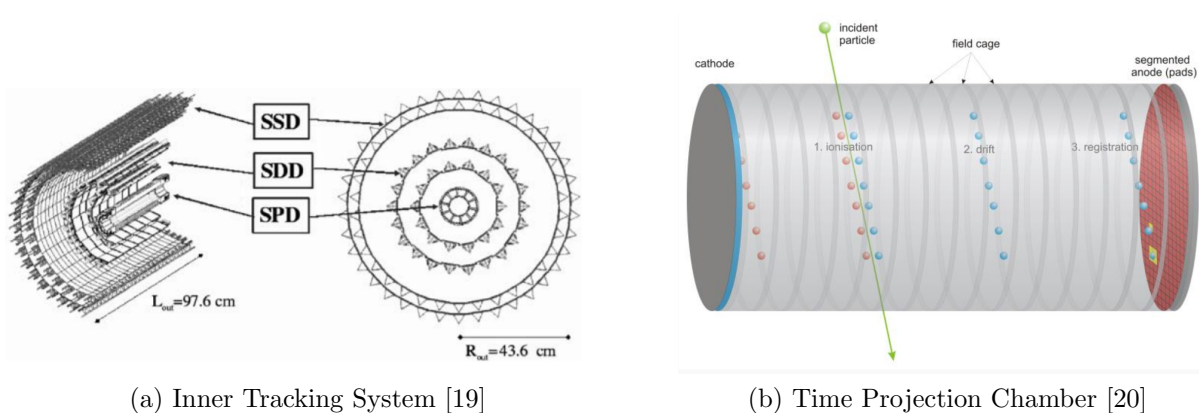
Figure 7: Schematic views on the ITS and TPC

The ITS is surrounded by the Time Projection Chamber (TPC)[21]. This detector is split in two chambers by a central cathode. A charged particle crossing the TPC ionises the gas along its path. The freed electrons will drift to the endplates in the TPC due to the electric field inside. From the signal the trajectory and momentum can be determined together with identification of the crossing particle. A visualisation of the process can be seen in figure 7.

---

[3]$\eta \equiv -\ln\left[\tan\left(\frac{\theta}{2}\right)\right]$ with θ the angle relative to the beam axis.

Both the ITS and TPC are surrounded by a magnet providing a 0.5T magnetic field inside the central barrel, making them the two main charged-particle tracking detectors in ALICE.

The last sub-system considered here is the V0 [22]. It consists of two forward scintillator arrays V0A and V0C positioned on opposite sides of the interaction point (see figure 8), covering pseudorapidity ranges $2.8 < \eta < 5.1$ and $-3.7 < \eta < -1.7$. In pp-collisions the V0 is used as a minimum bias trigger and can distinguish collisions between the two beams from background events like collisions with residual gas particles in the beam pipe. It also measures charged particle multiplicity, azimuthal distributions and beam luminosity.
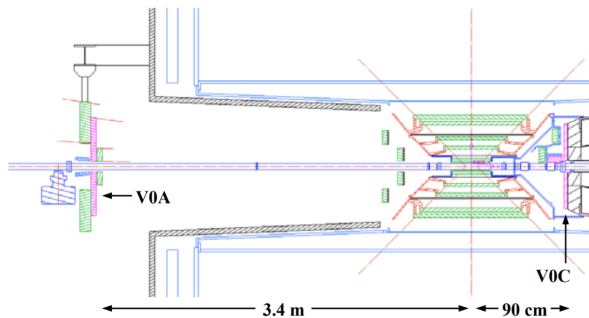

Figure 8: Location and schematic view on the two V0 detectors.[23]

3.2 Event and Track Selection

The trigger for a minimum bias event required a coincident signal in both the V0 detectors. The event is reconstructed in three phases using information from both the ITS and TPC. The first phase starts at the outer radius of the TPC from where the tracks are projected inwards through the ITS to the primary vertex. The next phase moves outward again using the clusters found in the first phase to identify different particle species. The third phase is an inward refit on the reconstructed tracks and expands the best fitted tracks to the primary vertex to fix their DCA. [24]

For this analysis only charged particle tracks with transverse momentum $0.2 < p_\mathrm{T} < 10\mathrm{GeV}/c$ and pseudorapidity range $|\eta| < 0.8$ are used. In the process of reconstruction a minimum of 70 TPC clusters (out of 159) is required for all tracks to pass and for each track a fraction of 0.4 shared clusters is allowed in the TPC. For the fitting in the third phase a maximal value of 36 is set for the χ^2 in the ITS and TPC per cluster constrained to a global track starting at the primary vertex. Only tracks with a distance of closest approach (DCA) to the primary vertex of maximal 2.4 cm in the x,y-plane and 3.2 cm in the z-direction were selected. With these criteria primary tracks with hits in both ITS and TPC detector as well as tracks only detected in the TPC will be reconstructed and used in the analysis.

This resulted in three data samples of 152, 230 and 296 million events that passed the event selection criteria and are used in this analysis.
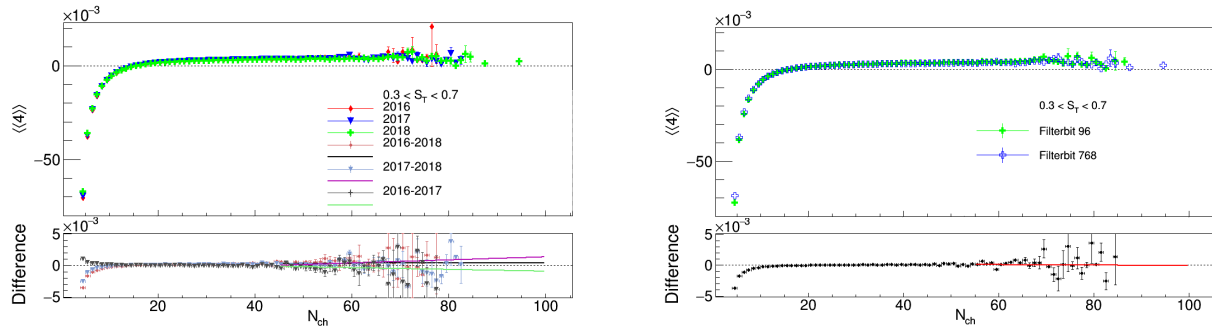
(a) The lines below the differences in the legend (2016-2018 reads 2016 minus 2018) represent the corresponding fits.

(b) Filterbit 768 represents the selection criteria described in section3.2 and 96 in section3.3.

Figure 9: Comparison for the 4-particle correlation at mid sphericity of the three datasets in (a) and selection criteria in (b).

3.3   Systematic Uncertainties

The systematic uncertainties are obtained by comparing the data measured for two different sources, all as a function of charged particle multiplicity. The first source consist of samples measured in different periods with similar selection criteria and the second of one sample analysed twice with different selection criteria. The process for determining the systematic uncertainties for both sources is almost identical and is summarized first.

	Independent	Completely Correlated
σ_{A-B}	$\sqrt{\sigma_A^2 + \sigma_B^2}$	$\sqrt{|\sigma_A^2 - \sigma_B^2|}$

Table 1: The propagation of statistical uncertainties for datasets A with statistical uncertainty σ_A and B with σ_B if the difference is taken.

The data is compared by taking the difference between all samples forming a source. In this process the propagation of statistical errors, see table 1, changes for completely correlated or independent datasets [25]. In this analysis measurements on the same events are assumed to be completely correlated and measurements on different events as independent. Global differences with the same sign larger than σ_{A-B} will directly be considered as systematic uncertainties (see $N_{ch} < 10$ in figure 9). If many points are distributed around zero the multiplicity dependence of the difference is fit by a linear function from which the global difference will be extracted ($N_{ch} > 50$). The final uncertainty for each source will be the absolute value of half the difference extracted from the fit or taken direct. By adding the uncertainties from both sources in quadrature the total systematic uncertainty is obtained.

For the first source three data samples containing all events from LHC runs in 2016, 2017 and 2018, reconstructed in agreement with the selection criteria summarised in section 3.2 were compared. The global difference between the most deviating periods was taken to extract the systematic uncertainty. The selection criteria for the second source are summarized in

section 3.2. The criteria for the second analysis were modified to a tight p_T dependent DCA cut (decreasing for an increasing p_T) extended with tracks requiring a hit in the SDD and no hits in the SPD[24]. This resulted in two sets of three samples which are finally merged, both separately, into one sample describing the same events in the period 2016-2018. As can be seen in figure 9 both sources contribute around a maximum of 5% at the lowest multiplicity bins to the systematic uncertainties and therefore will be used to determine its total value.

3.4   Model

Monte Carlo generators are widely used to describe high energetic proton-proton collisions like the ones performed at the LHC. A comparison between experimental data and these event simulations provides information about the underlying physics. In this analysis two configurations of PYTHIA8[26] are used as event simulators. They both describe proton-proton collisions at a centre of mass energy $\sqrt{s} = 13$TeV and generate about two billion events. For one of the simulations a method for colour reconnection is incorporated in PYTHIA8, for the other it is switched of.

The PYTHIA8 model describes the physics of hard processes, parton showers, particle decays, multiparton interactions, beam remnants and string fragmentation in a collision. The most important feature for this analysis is that PYTHIA8 does not include any hydrodynamical models for the collisions, this means no QGP is created in these simulations. This means that the collective behaviour discovered in small collision systems cannot be generated in the PYTHIA8 simulations, if the QGP is its only source. However, the PYTHIA8 model can be tuned with a mechanism that is able to reproduce some of the flow-like patterns observed in pp-collisions, called colour reconnection [27]. To test whether the addition of colour reconnection improves the PYTHIA8 model performance, it will be presented alongside the regular tune and both will be compared to the data.

3.4.1   Colour Reconnection

Colour reconnection describes a process at parton (quarks and gluons) level before hadronization takes place after the collision. Multi parton interactions (MPI) lead to quarks being kicked out of their initial bound state, making the colour tubes that connect them lengthen in the process, ending in many overlapping colour tubes in space. The model of colour reconnection rearranges the colour tubes between the scattered quarks in such a way that the quarks are connected to their new nearest 'neighbours' and this reduces the total tube length. This causes a decrease in potential energy between the quarks (confinement) and generates an increase in average transverse momentum. More MPI means more energy is gained by colour reconnection and will result in a higher mean p_T boost for high multiplicities[28]. The extra energy needed to create this p_T boost is compensated by a decrease in the number of final state particles created in the collision. The same kind of multiplicity dependent p_T boost is present in heavy ion collisions where it is a consequence of the formation of a QGP.

4   Results and Discussion

The charged particle multiplicity dependence of multi-particle correlations, cumulants and second harmonic flow coefficients at $\sqrt{s} = 13\text{TeV}$ measured in pp-collisions is presented along with predictions of the PYTHIA8 model tuned with and without colour reconnection.

All data in this chapter, except section 4.5, is presented as follows. The statistical uncertainties are shown as vertical lines for the data and filled bands for the models. The horizontal line for each data point covers two multiplicity bins. The systematic uncertainties in the data samples are visualized as blank boxes. The PYTHIA8 tune with colour reconnection tuned on, referred to as PYTHIA8+CR, is purple coloured in all graphs and the tune without colour reconnection, PYTHIA8, is presented in green.

First the results for the inclusive analysis are presented and discussed followed by the results for low, mid and high sphericity. The results are extended with a discussion on the reconstruction of inclusive results from the low, mid and high sphericity results.

4.1   Inclusive Sphericity

4.1.1   Correlations

In figure 10 the results from the multi-particle azimuthal correlations up to eight order are shown. All correlation functions show qualitatively similar multiplicity dependences with a peak around 10 charged particles followed by a decrease in magnitude before approaching a saturation value at which the magnitudes stay more or less constant for increasing multiplicities.

The multiplicity dependence of $\langle\langle 2\rangle\rangle$ is shown in figure 10a and stabilizes around $N_{ch} = 50$ at a magnitude of 0.02, 30% beneath the maximum value reached at $N_{ch} \approx 10$. Above $N_{ch} \approx 70$ the increasing statistical uncertainties cause the data to fluctuate heavily and complicate the analysis. The azimuthal correlations drop an order of magnitude when four particles are considered, shown in figure 10b. After $\langle\langle 4\rangle\rangle$ reached its peak the magnitude decreases to more than half its maximum value and saturates around 0.8×10^{-3}. The statistical uncertainties again prevent a clear view for $N_{ch} > 70$, however above $N_{ch} = 80$ the data does seem to get consistent with zero. When again an order of magnitude is dropped the magnitudes of $\langle\langle 6\rangle\rangle$ are reached, see figure 10c, with a peak value of 2.4×10^{-4} and a saturation magnitude around 0.8×10^{-4}, however $\langle\langle 6\rangle\rangle$ quickly attenuates further before the fluctuations due to statistical uncertainties become significant. At multiplicities above 80 the data is again consistent with zero. The last plot, figure 10d, shows the multiplicity dependence of $\langle\langle 8\rangle\rangle$, again with smaller magnitudes compared to the lower order correlations. The maximum value is around 5×10^{-5} followed by a more fluctuating attenuation compared to the lower order correlations and continues this trend, through statistical fluctuations, to become consistent with zero around $N_{ch} = 80$.

Both PYTHIA8 tunes are in qualitative agreement with the data and describe the same multiplicity dependence with a peak at low multiplicities followed by a decline until the saturation values are reached and the models stay constant until the CR-tune also starts to fluctuate. The regular tune does not show any significant fluctuations due to the larger statistics at high
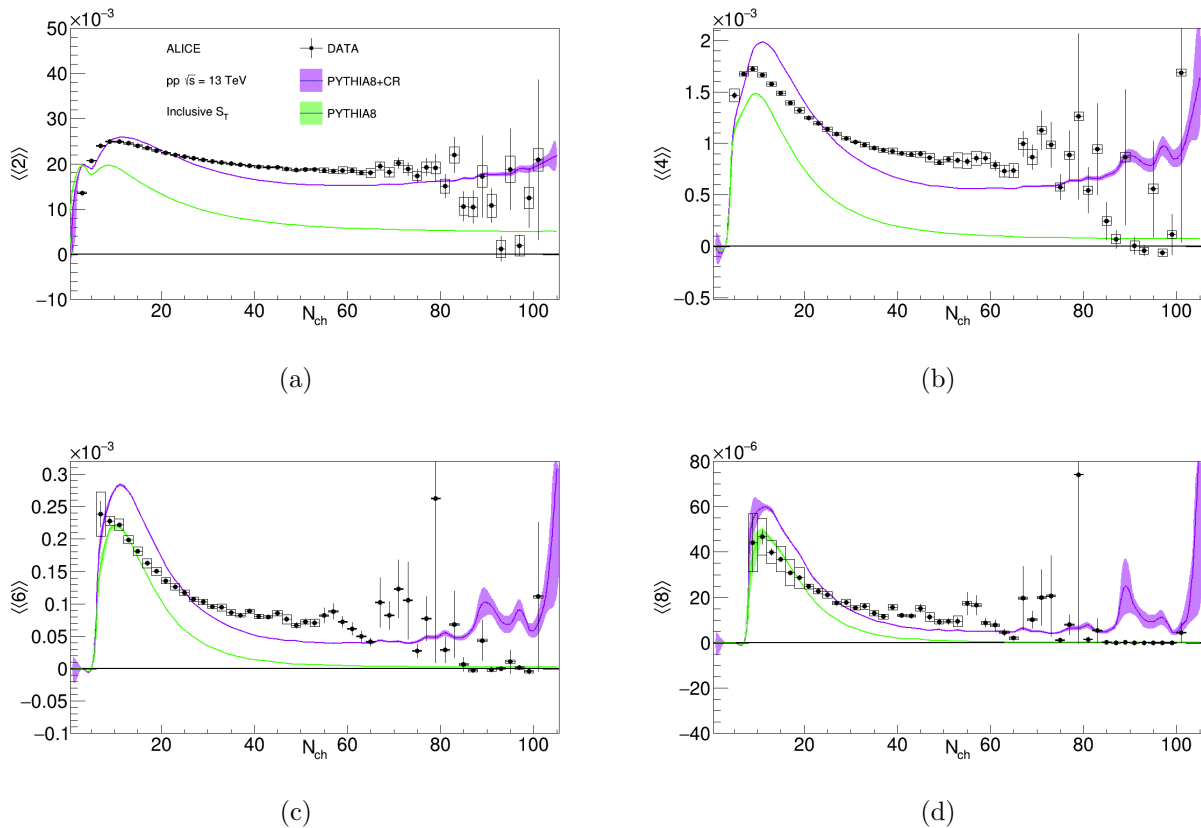
Figure 10: The charged particle multiplicity dependence of $\langle\langle 2 \rangle\rangle$, $\langle\langle 4 \rangle\rangle$, $\langle\langle 6 \rangle\rangle$ and $\langle\langle 8 \rangle\rangle$, in the inclusive analysis of pp-collisions.

multiplicities. Besides following the same trend, both models do exhibit some quantitative differences. The CR-tune is in better agreement with the $\langle\langle 2 \rangle\rangle$ data for all multiplicities. For the higher order correlations, the CR-tune is performing better for $25 < N_{ch} < 80$ giving a closer estimate on the plateaus as well. However, above $N_{ch} = 80$ the correlations, especcially $\langle\langle 6 \rangle\rangle$ and $\langle\langle 8 \rangle\rangle$, attenuate to zero and are consistent with the regular tune. The CR-tune overestimates the peaks for $N_{ch} < 25$, where the regular tune underestimates $\langle\langle 4 \rangle\rangle$ but is in quantitative agreement with $\langle\langle 6 \rangle\rangle$ and $\langle\langle 8 \rangle\rangle$ up to 16 and 20 charged particles, respectively. The correlation functions decrease significantly for each higher order, as expected since non-flow contributions arise from few-particle correlations and are most dominant in $\langle\langle 2 \rangle\rangle$.

4.1.2   Cumulants

To determine whether the azimuthal correlations describe global anisotropies and indicate the formation of a QGP, the cumulants are analysed as well, since anisotropic flow requires both $c_2\{2\}$ and $c_2\{6\}$ to be positive while $c_2\{4\}$ and $c_2\{8\}$ to be negative.

The multiplicity dependence of $c_2\{2\}$, $c_2\{4\}$, $c_2\{6\}$ and $c_2\{8\}$ is shown in figure 11. All four cumulants have a positive sign and become consistent with zero for increasing multiplicities with the negative values for $c_2\{4\}$ and $c_2\{8\}$ reached at multiplicities above 80 not to be
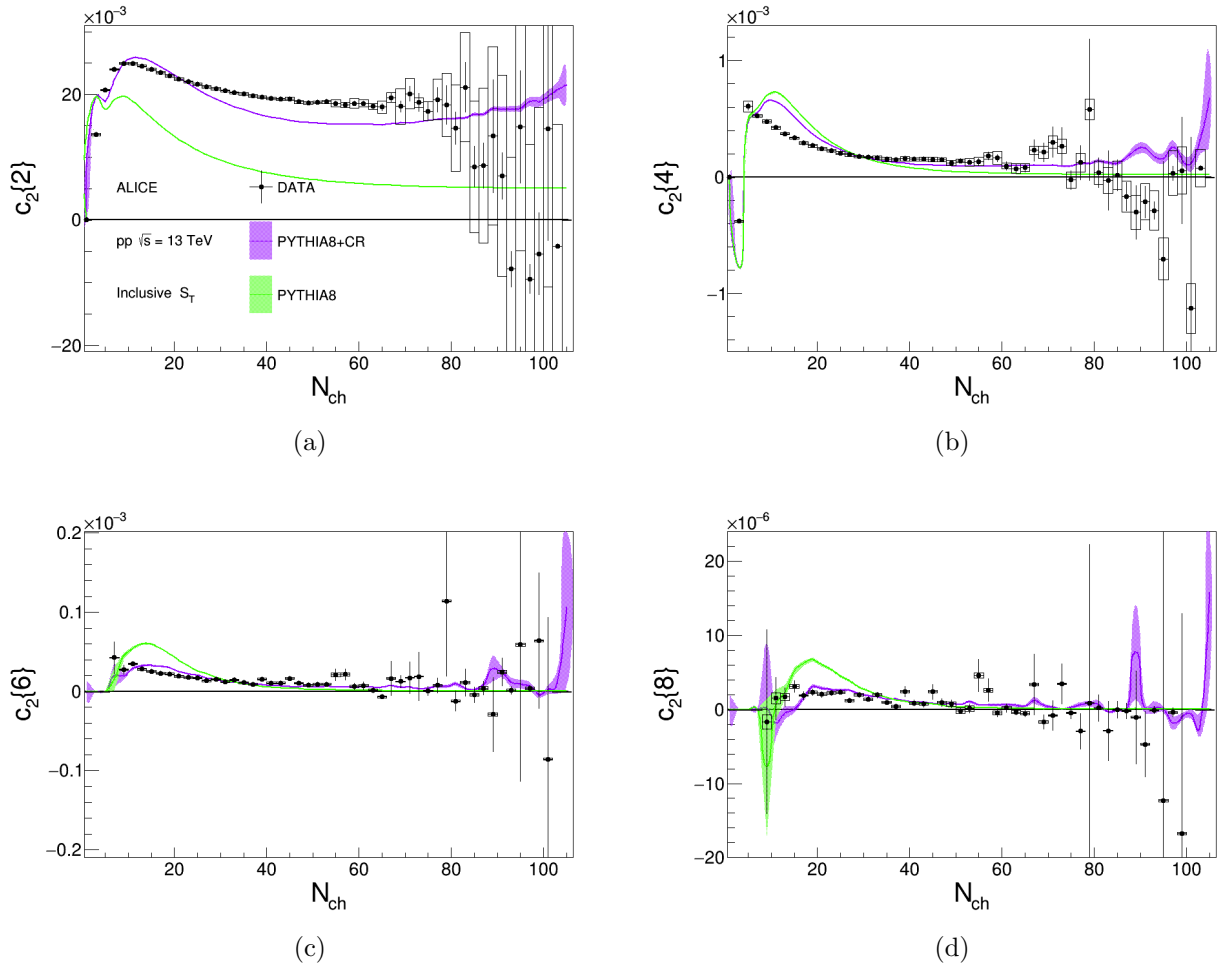
Figure 11: The charged particle multiplicity dependence of $c_2\{2\}$, $c_2\{4\}$, $c_2\{6\}$ and $c_2\{8\}$ in the inclusive analysis of pp-collisions.

interpreted as collective flow but rather as a consequence of statistical fluctuations.

The multiplicity dependence of $c_2\{2\}$ should be, by definition, similar to $\langle\langle 2 \rangle\rangle$. Figure 11a is exactly the same as $\langle\langle 2 \rangle\rangle$ up to $N_{ch} = 70$ where the systematic uncertainties for $c_2\{2\}$ suddenly increase, caused by the additional datapoints that appear at negative values. These could arise from uncertainties in the determination of $\langle\langle 2 \rangle\rangle$ or $c_2\{2\}$. The model performances do stay similar for all N_{ch}. All three higher order cumulants are, as expected, reduced in magnitude compared to the higher order correlations. They still follow the same trend with a peak at $N_{ch} \approx 10$ followed by an attenuation until $c_2\{4\}$ and $c_2\{6\}$ reach their saturation values and stay constant up to $N_{ch} \approx 60$ where the statistic fluctuations become significant and the data gets consistent with zero. The same trend is followed by $c_2\{8\}$, only the more significant statistic fluctuations complicate to determine whether a plateau is reached.

Both PYTHIA8 tunes describe the same sign distribution as the data. Both tunes overestimate the peak for $c_2\{4\}$ by shifting its maximal value to $N_{ch} = 12$ instead of $N_{ch} = 4$. The

CR-tune again gives a better estimate on the plateau. Both $c_2\{6\}$ and $c_2\{8\}$ are in quantitative agreement with the CR-tune independent of multiplicity, where the regular tune still overestimates the peak at low N_{ch}.

The positive signs for $c_2\{4\}$ and $c_2\{8\}$, do not allow real valued estimates on v_2 and therefore do not provide any sign that the multi particle correlations observed in the pp-collisions in this multiplicity range are caused by collective flow. The PYTHIA8+CR model tune, which is in qualitative and for $c_2\{6\}$ and $c_2\{8\}$ even quantitative agreement with the data, supports this statement.

Thus, without any selection on final state topologies no signs of collectivity are observed in the multiplicity range presented here. This leads to the next step where the tools presented on event shape engineering can be used to split up the inclusive results and analyse the results for low, mid and high sphericity separately to see whether their final state topologies introduce any collective flow like effects.

4.2   Low Sphericity

4.2.1   Cumulants

Figure 12 shows the multiplicity dependence of $c_2\{2\}$, $c_2\{4\}$, $c_2\{6\}$ and $c_2\{8\}$ for all events having $0.0 < S_T < 0.3$. In contrast to the inclusive results the cumulants now exhibit the sign distribution which allows for real valued estimates of v_2, with a positive sign for $c_2\{2\}$ and $c_2\{6\}$, but a negative sign for both $c_2\{4\}$ and $c_2\{8\}$. Besides, all cumulants cover the same order of magnitude in contrast to the inclusive results which decreased for each higher order cumulant.

The positive valued $c_2\{2\}$ and $c_2\{6\}$ start at a maximum value followed by a decrease until $N_{ch} \approx 20$ where the curves flatten at values of 0.3 and 0.12 respectively and remain constant for increasing multiplicities up to $N_{ch} \approx 40$. For $40 < N_{ch} < 60$ the curve of $c_2\{2\}$ slightly attenuates where $c_2\{6\}$ clearly rises. Above $N_{ch} = 60$ no data is present for $c_2\{6\}$, while $c_2\{2\}$ does provide measurements in this range. They seem to arise from some single counts of low sphericity events with $N_{ch} > 60$, see figure 6. The lack of statistical uncertainties for these points supports the assumption, however it is not clear why these measurements are absent for $c_2\{6\}$. Both $c_2\{4\}$ and $c_2\{8\}$, with negative signs, increase to values of -0.1 and -0.31 respectively and remain constant for higher multiplicities within the same ranges as $c_2\{2\}$ and $c_2\{6\}$. Increasing the multiplicity above $N_{ch} \approx 40$ leads to a slight increase in $c_2\{4\}$ and a more evident decrease for $c_2\{8\}$. The measurements above $N_{ch} = 60$ again only appear in $c_2\{4\}$ explained conform $c_2\{2\}$ and $c_2\{6\}$.

Both PYTHIA8 tunes are in qualitative agreement with the data and predict all signs correctly, which provides compelling evidence for the non-collective origin of this sign distribution. The tunes provide almost equivalent estimates up to $N_{ch} \approx 20$, describing a slightly higher peak for $c_2\{2\}$ and $c_2\{6\}$ and more negative peak values for $c_2\{4\}$ and $c_2\{8\}$. For $N_{ch} > 20$ the CR-tune attenuates more gradually and predicts a saturation value in agreement with both $c_2\{2\}$ and $c_2\{4\}$ and reduces the difference between the model and data around 50% for the other cumulants when compared to the regular tune.
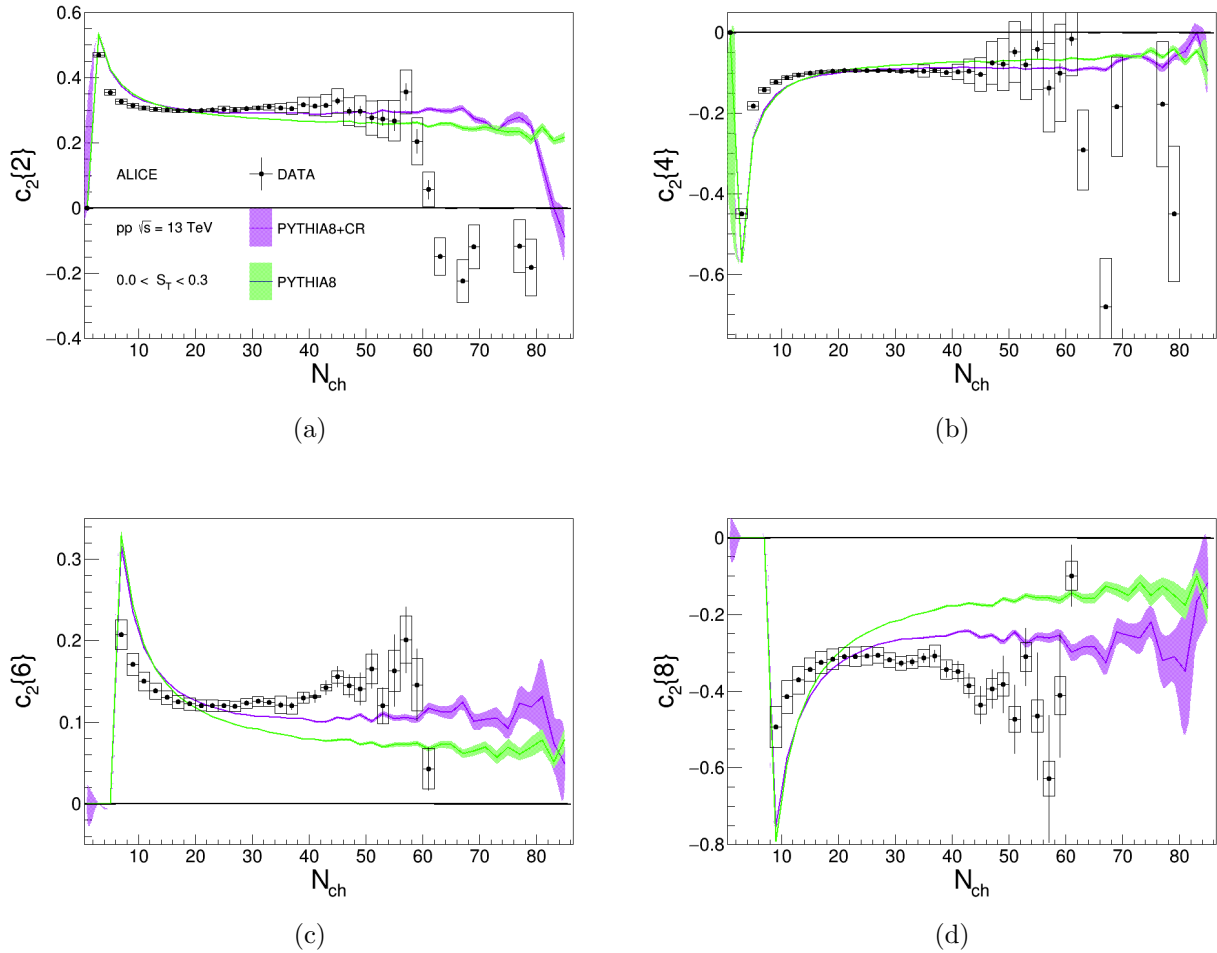
Figure 12: The multiplicity dependence of $c_2\{2\}$, $c_2\{4\}$, $c_2\{6\}$ and $c_2\{8\}$ measured in low sphericity pp-collisions.

4.2.2   Eliptic Flow Coefficients

The low sphericity cumulants allow real valued estimates on v_2, which should not be interpreted as a quantification of elliptic flow, but mainly as the contribution of bias created by selection of low sphericity events to the measurements of v_2.

The multiplicity dependence of $v_2\{m\}$ determined from $c_2\{m\}$, with $m = 2, 4, 6, 8$ and following equation 8, is shown in figure 13. All four graphs are displayed with an additional dashed red line at identical values to clearly visualise how the different cumulants estimate similar values for v_2. The multiplicity dependence of $v_2\{m\} \propto \sqrt{c_2\{m\}}$ for $m = 2, 6$ and $v_2\{m\} \propto \sqrt{-c_2\{m\}}$ for $m = 4, 8$ and therefore do not need to be discussed here again in detail, since they follow qualitatively the same trends with $v_2\{4\}$ and $v_2\{8\}$ changing their sign and no major differences in model performances are observed as well.
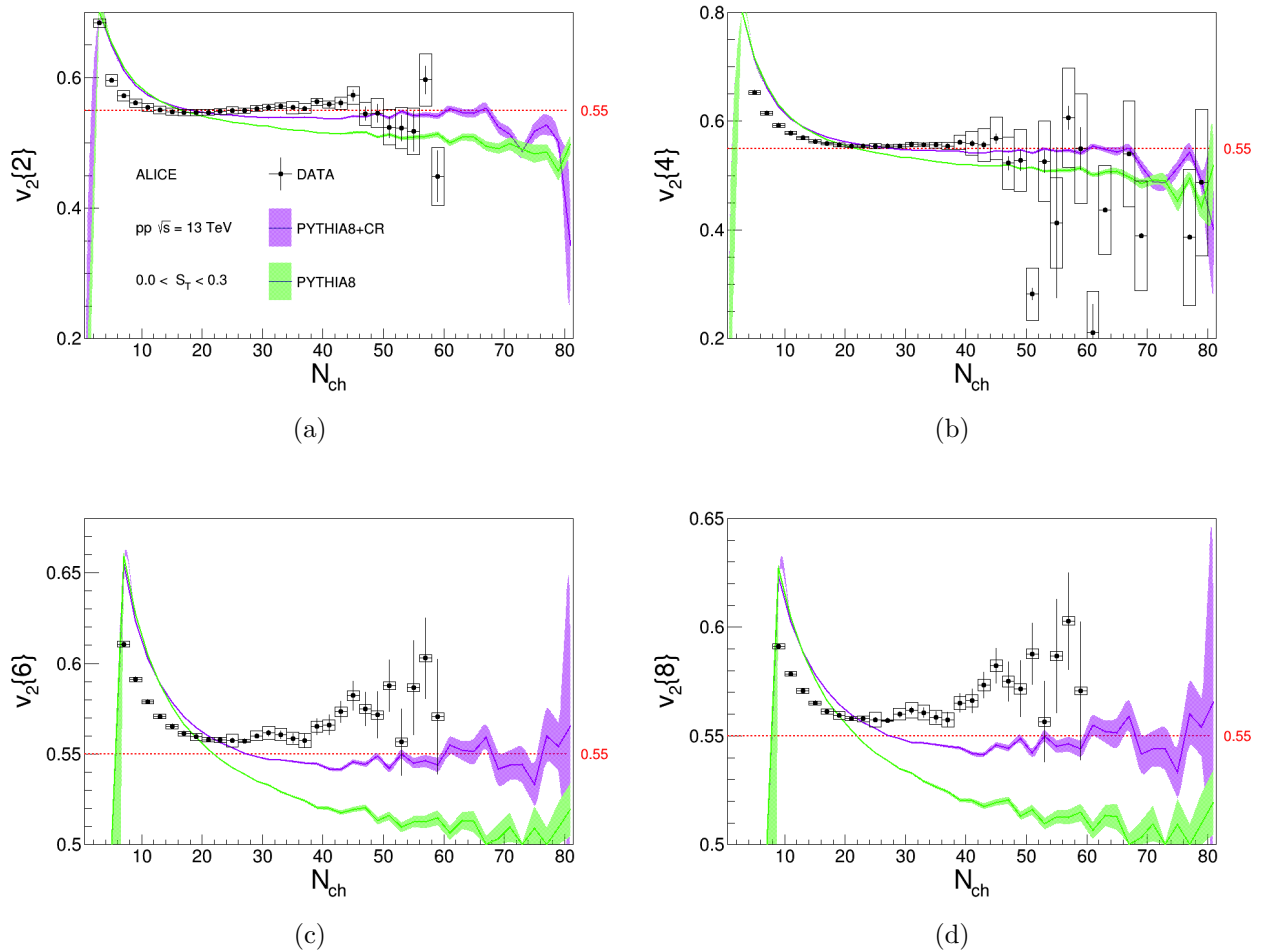
Figure 13: The multiplicity dependence of $v_2\{2\}$, $v_2\{4\}$, $v_2\{6\}$ and $v_2\{8\}$ measured in low sphericity pp-collisions.

The importance of this figure is displayed in the saturation value of roughly 0.55 for all estimates on v_2 and a peak value around 0.7 at the lowest multiplicity bins, both in qualitative agreement with the data. The reached values for v_2 are quite high when compared to the upper limit of $v_2\{m\} = 0.1$ in Pb-Pb collisions [9]. This shows how the bias created by selecting only low sphericity final state topologies generates strong v_2 values and contributes significantly to inclusive v_2 measurements in the low multiplicity range where these sphericity events are dominant.

4.3 Mid Sphericity

4.3.1 Cumulants

Figure 14 shows the multiplicity dependence of $c_2\{2\}$, $c_2\{4\}$, $c_2\{6\}$ and $c_2\{8\}$ for all events having $0.3 < S_T < 0.7$. The cumulants in this multiplicity and sphericity range show the same sign distribution as the low sphericity measurements, with $c_2\{2\}$, $c_2\{4\} > 0$ and $c_2\{6\}$,
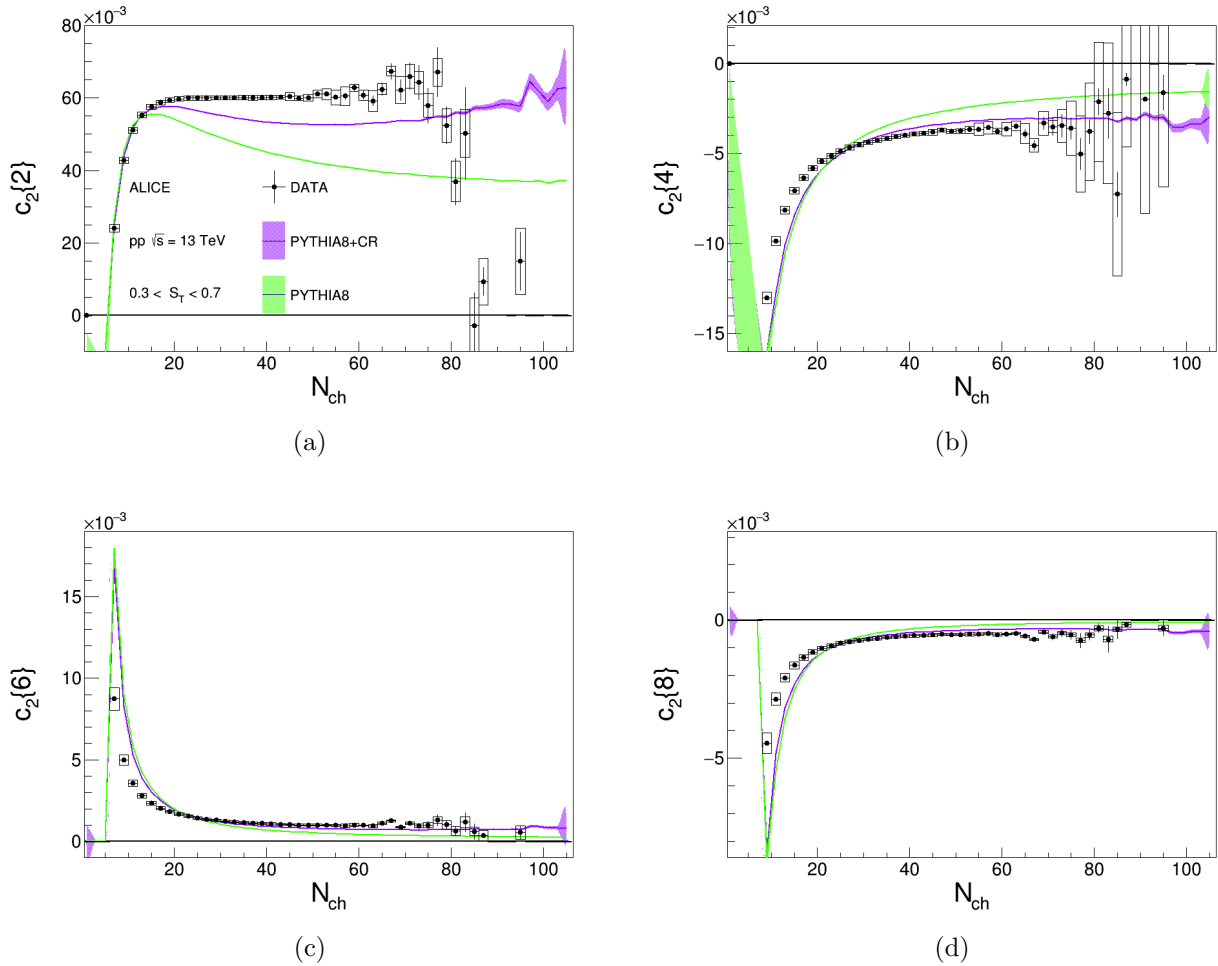
Figure 14: The multiplicity dependence of $c_2\{2\}$, $c_2\{4\}$, $c_2\{6\}$ and $c_2\{8\}$ measured in mid sphericity pp-collisions.

$c_2\{8\} < 0$. However, in contrast to the low multiplicity cumulants, where all magnitudes were of the same order, the mid sphericity $c_2\{4\}$ plateau at -5×10^{-3} is decreased an order of magnitude compared to $c_2\{2\}$ around 6×10^{-2} with even lower magnitudes of 1×10^{-3} and -1×10^{-3} for $c_2\{6\}$ and $c_2\{8\}$ respectively. The plateaus are reached at $N_{ch} \approx 20$ after a steep decline towards zero for $c_2\{4\}, c_2\{6\}$ and $c_2\{8\}$ while $c_2\{2\}$ rises from zero towards the saturation value. All four plateaus remain stable up to $N_{ch} \approx 60$. For $N_{ch} > 60$ the fluctuations due to smaller statistics become more significant and complicate any further analysis. Only the systematic uncertainties for $c_2\{2\}$ and $c_2\{4\}$ increase quickly in this regime, which arise most likely from the same single measurements as were observed in the low sphericity $c_2\{2\}$ and $c_2\{4\}$.

Both PYTHIA8 tunes describe the right signs for all four cumulants and are in agreement with the $c_2\{2\}$ data until $N_{ch} \approx 15$ where the data remains constant but both tunes decrease for higher multiplicities, 15% lower for the CR-tune compared to 30% for the regular tune. For the higher order cumulants both tunes overestimate all peaks present in the lowest multiplicity bins in the range $0 < N_{ch} < 20$ after which the models and data intersect. After intersec-
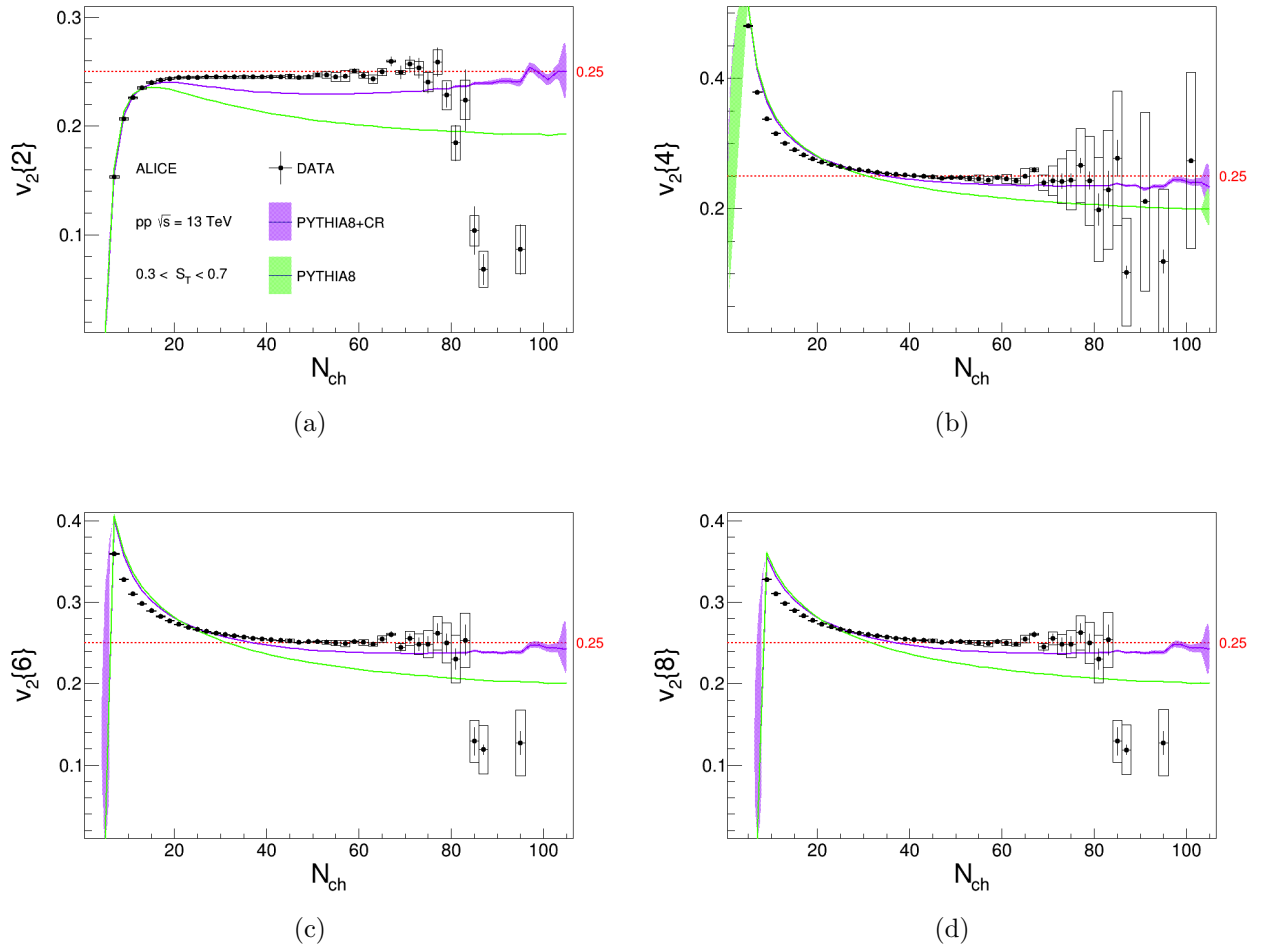
Figure 15: The multiplicity dependence of $v_2\{2\}$, $v_2\{4\}$, $v_2\{6\}$ and $v_2\{8\}$ measured in mid sphericity pp-collisions.

tion, the models continue to decline while the data becomes constant resulting in increasing disagreements for higher multiplicities, with the CR-tune maintaining the smallest difference for all cumulants.

The measurements, supported by the consistent model performances, show once more how the bias introduced by selection on final state topologies, this time for mid sphericity events, causes all cumulants to show signs of collective flow.

4.3.2   Eliptic Flow Coefficients

The results again allow real valued estimates on v_2 from all four cumulants and can give insight on the contribution of mid sphericity event shapes to v_2. Figure 15 shows the multiplicity dependence of $v_2\{2\}$, $v_2\{4\}$, $v_2\{6\}$ and $v_2\{8\}$ with the red dashed line indicating the consistent saturation values. This value of 0.25 is less than half the magnitude reached in the low sphericity events. This decrease is in line with the assumption that event shapes generate v_2, since the mid sphericity events result from selecting more isotropic particle distributions, which reflect
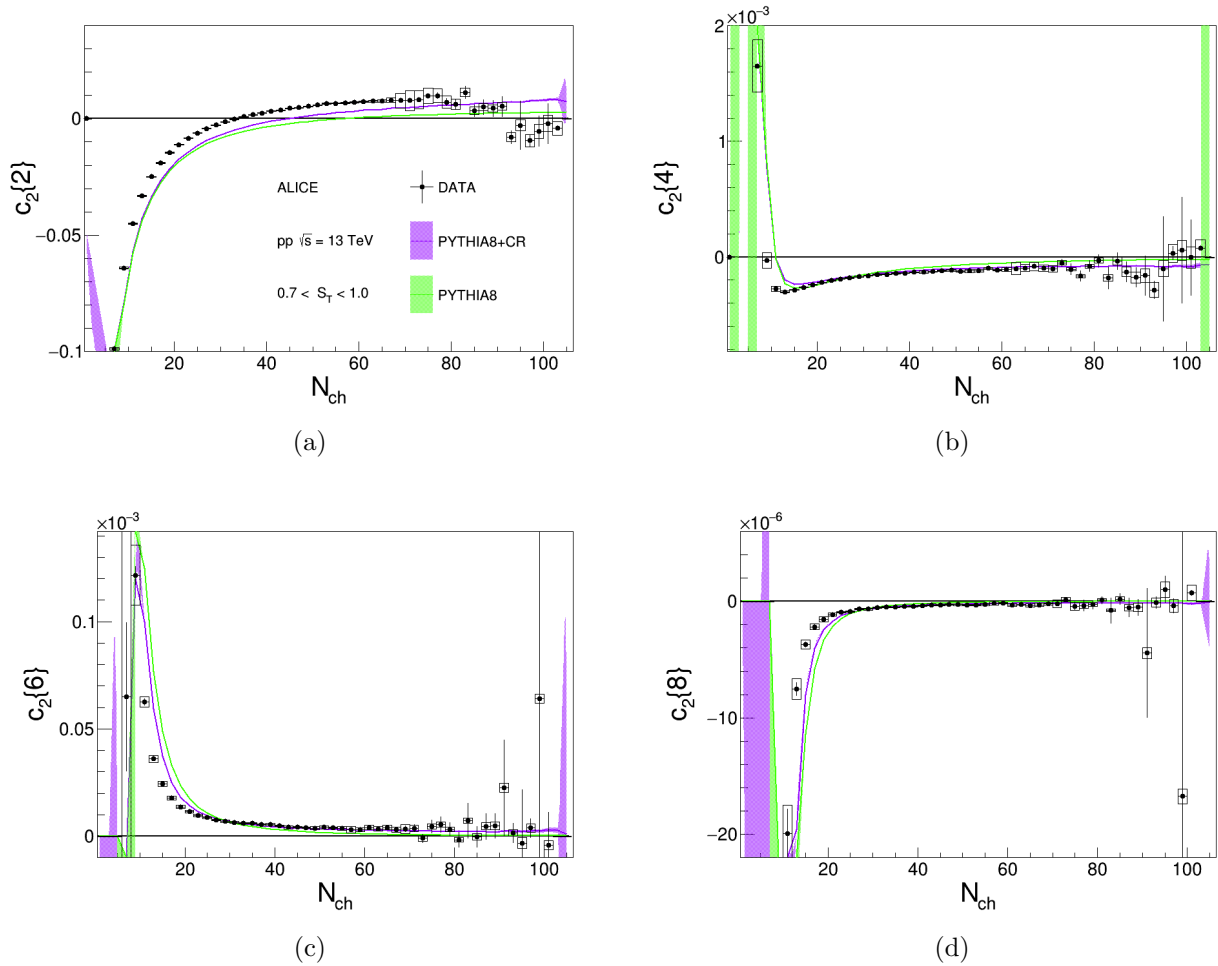
Figure 16: The multiplicity dependence of $c_2\{2\}$, $c_2\{4\}$, $c_2\{6\}$ and $c_2\{8\}$ measured in high sphericity pp-collisions.

less ellipticity by definition.

Although the saturation value has significantly decreased, it is still quite large when compared to the maximum of 0.1 reached in Pb-Pb collisions and this bias can therefore still be seen as a generator of v_2. However, it is more complicated to see the contribution of mid sphericity events in the inclusive analysis since there is no multiplicity regime where mid sphericity events are most dominant.

4.4 High Sphericity

4.4.1 Cumulants

The high sphericity events consist of the most isotropic events and are therefore expected to reflect little to none bias generated by their event shapes. Figure 16 shows the multiplicity dependence of $c_2\{2\}$, $c_2\{4\}$, $c_2\{6\}$ and $c_2\{8\}$ for all events having $0.7 < S_T < 1.0$. Even in this sphericity regime the cumulants reach their saturation values with the same sign distribution

as the low and mid sphericities, only $c_2\{2\}$ starts out negative and changes sign at $N_{ch} \approx 35$ and prohibits the subtraction of a real valued $v_2\{2\}$ below this multiplicity. All four cumulants are again highly sensitive to increasing multiplicities below $N_{ch} \approx 20$ and now saturate at even smaller values when compared to the inclusive result, with a saturation value around $N_{ch} = 60$ of approximately 0.01 for $c_2\{2\}$, -1×10^{-3} for $c_2\{4\}$, 2×10^{-6} for $c_2\{6\}$ and even -1×10^{-7} for $c_2\{8\}$. Above $N_{ch} \approx 80$ all cumulants get consistent with zero and fluctuate due to the limited statistics. The systematic uncertainties only increase slightly for the lowest and highest multiplicities however, do not play a significant role in this sphericity range.

The PYTHIA8 model tunes are again in qualitative agreement with all cumulants, describing the same signs and trends. However, the sing change for $c_2\{2\}$ is predicted at higher multiplicities by both models, due to their slightly lower trends compared to the data, with the CR-tune changing sign at $N_{ch} \approx 45$ and the regular tune at $N_{ch} \approx 57$. The model predictions on the higher order cumulants are mainly in quantitative agreement with the data. Both tunes slightly underestimate the steep declines at the lowest multiplicities but do predict consistent peak values. Above a multiplicity of $N_{ch} \approx 30$ the CR-tune is in quantitative agreement with the experimental results in the presented multiplicity range while the regular tune underestimates all plateaus.

Even in this high sphericity regime, where the event shapes cannot generate high v_2 values, the cumulants still show signs of collective flow. The PYTHIA8 models are able to follow this trend with the CR-tune even in quantitative agreement with $c_2\{4\}$, $c_2\{6\}$ and $c_2\{8\}$ for high multiplicities. This again proves how the cumulant distribution does not necessarily need the formation of a QGP but can be generated by selection on the final state event shape, independent for low, mid or high sphericity.

4.4.2 Eliptic Flow Coefficients

The high sphericity cumulants described in the previous section allow again for real valued estimates of v_2, with the exception of $v_2\{2\}$ below $N_{ch} \approx 35$. Figure 17 shows the multiplicity dependence of $v_2\{2\}$, $v_2\{4\}$, $v_2\{6\}$ and $v_2\{8\}$ with the red dashed line at a magnitude of 0.1 to point out the shared saturation value. The v_2 magnitudes reached here cannot simply be attributed to the event shapes, but the quantitative agreement of the CR-tune for both the cumulants and elliptic flow coefficients (only qualitative for $c_2\{2\}$ and $v_2\{2\}$) shows there is not necessarily QGP needed to generate these results as well. The results clearly show how an arbitrary selection on event shapes generates collective effects for all three sphericity regimes and can contribute to inclusive measurements. However, this can only be concluded for multiplicity ranges in which only low, mid or high sphericity events dominate.

It feels intuitively to think that the inclusive measurements on v_2 can be reconstructed from the sphericity binned results, however the results clearly show the opposite. The inclusive cumulants do not allow for real valued $v_2\{4\}$ and $v_2\{8\}$, where after a sphericity cut all cumulants allow real valued estimates of v_2. This raises the question how the inclusive results can be reconstructed from the sphericity binned results.
The reconstruction on cumulant level seems impossible as well, since both $c_2\{4\}$ and $c_2\{8\}$ show positive signs in the inclusive analysis and negative signs for low, mid and high spherici-
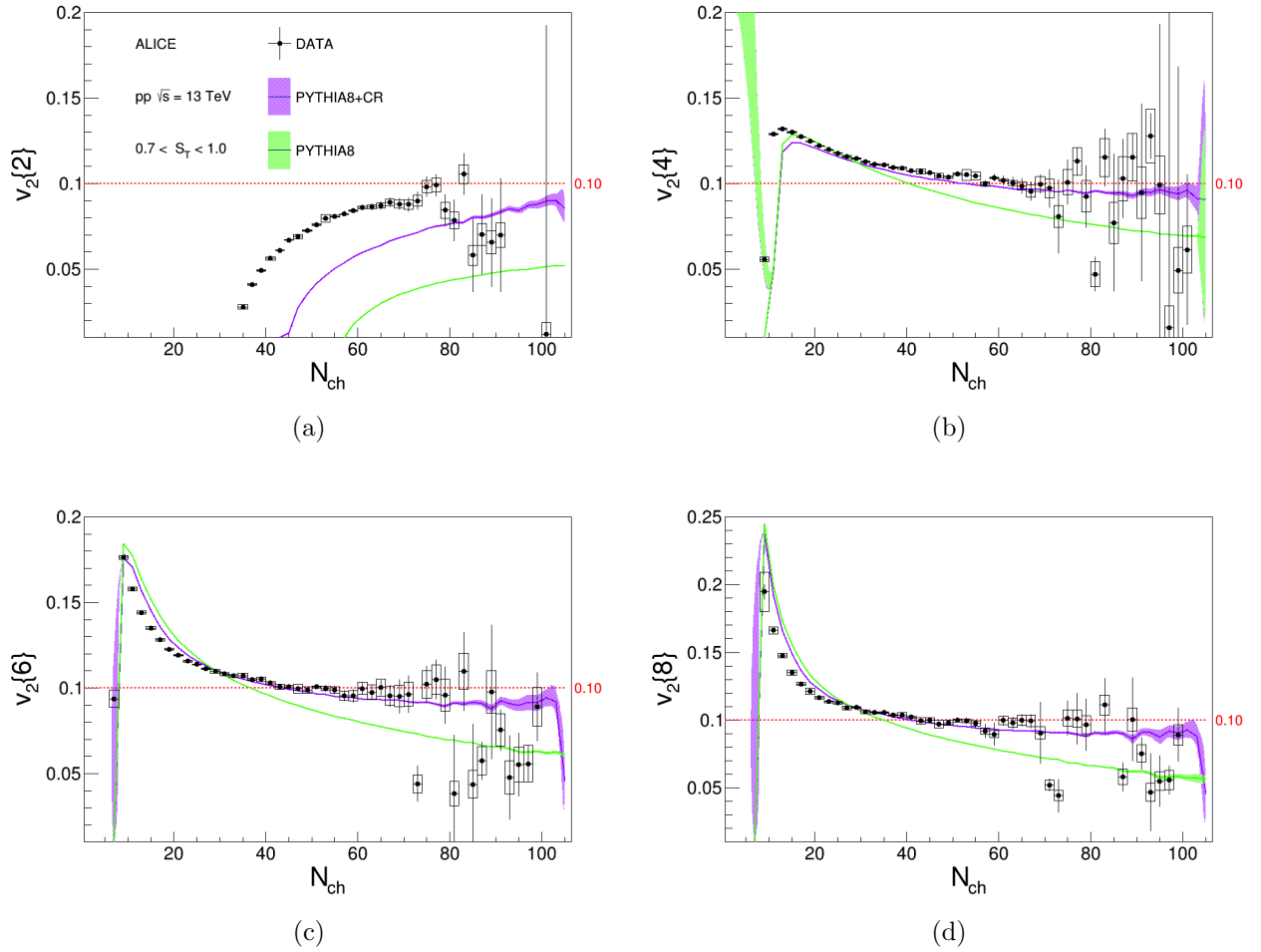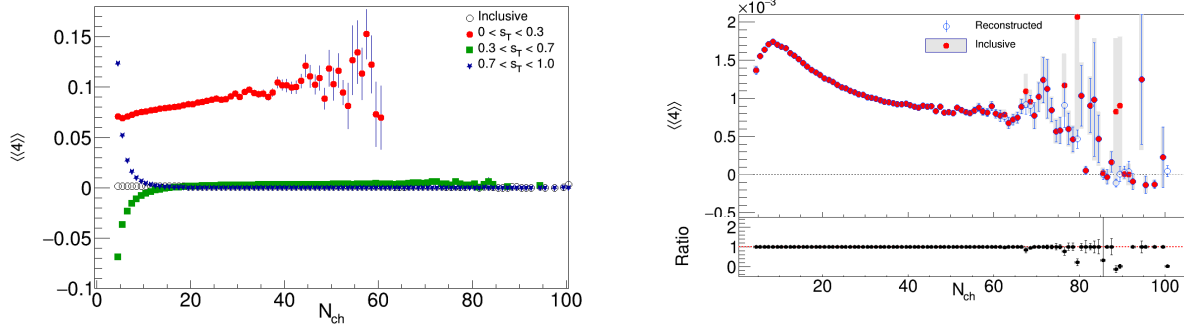
Figure 17: The multiplicity dependence of $v_2\{2\}$, $v_2\{4\}$, $v_2\{6\}$ and $v_2\{8\}$ measured in high sphericity pp-collisions.

ties. This is expected by the definitions of $c_2\{4\}$, $c_2\{6\}$ and $c_2\{8\}$, defined in equation 6 and 7. They involve higher powers of correlations and thus, cannot simply be added to reconstruct the inclusive results. Therefore, it is needed to look back at the correlations and reconstruct the inclusive results from there. The results from this analysis are presented in the next section.

4.5   Reconstruction of Inclusive Sphericity

In this section $\langle\langle 4 \rangle\rangle$ is used to demonstrate the analysis, the reconstruction of $\langle\langle 2 \rangle\rangle$, $\langle\langle 6 \rangle\rangle$ and $\langle\langle 8 \rangle\rangle$ can be found in the appendix.

The reconstruction of the inclusive correlation function is not simply the addition of low, mid and high sphericity binned results, as can be seen in figure 18 where this would result in a four particle correlation function with values around 0.1 for $N_{ch} < 60$, where the inclusive $\langle\langle 4 \rangle\rangle$ only reaches a maximum value around 2×10^{-3}.

(a) The multiplicity dependence of $\langle\langle 4 \rangle\rangle$ for the inclusive analysis together with the low, mid and high sphericity binned results.

(b) The multiplicity dependence of inclusive $\langle\langle 4 \rangle\rangle$ and the reconstructed $\langle\langle 4 \rangle\rangle$ with the low, mid and high sphericity binned results together with the ratio $\frac{Reconstructed}{Inclusive}$.

Figure 18: The multiplicity dependence of $\langle\langle 4 \rangle\rangle$.

The multiplicity binned histograms in figure 18a cannot directly be added since they are weighted, but with their weights included, reconstruction of the inclusive correlations is possible. The weighted four particle correlation function is defined as:

$$\langle\langle 4 \rangle\rangle \equiv \frac{\sum_{i=1}^{N}\left(W_{\langle 4 \rangle}\right)_i \langle 4 \rangle_i}{\sum_{i=1}^{N}\left(W_{\langle 4 \rangle}\right)_i}, \tag{11}$$

where the denominator is defined as the sum of event weights for N events and is visualized in figure 19a and figure 19b visalizes the numerator. The addition in figure 19a can be written as:

$$\sum W_{\langle 4 \rangle} = \sum W_{\langle 4 \rangle Low} + \sum W_{\langle 4 \rangle Mid} + \sum W_{\langle 4 \rangle High}, \tag{12}$$

where the sum runs over N and the subscript i is dropped for simplicity. The inclusive sum of event weights, according to figure 19b can be written as:

$$\sum W_{\langle 4 \rangle}\langle 4 \rangle = \sum W_{\langle 4 \rangle}\langle 4 \rangle_{Low} + \sum W_{\langle 4 \rangle}\langle 4 \rangle_{Mid} + \sum W_{\langle 4 \rangle}\langle 4 \rangle_{High}. \tag{13}$$

When equations 12 and 13 are combined to form equation 11, the inclusive result can be reconstructed as:
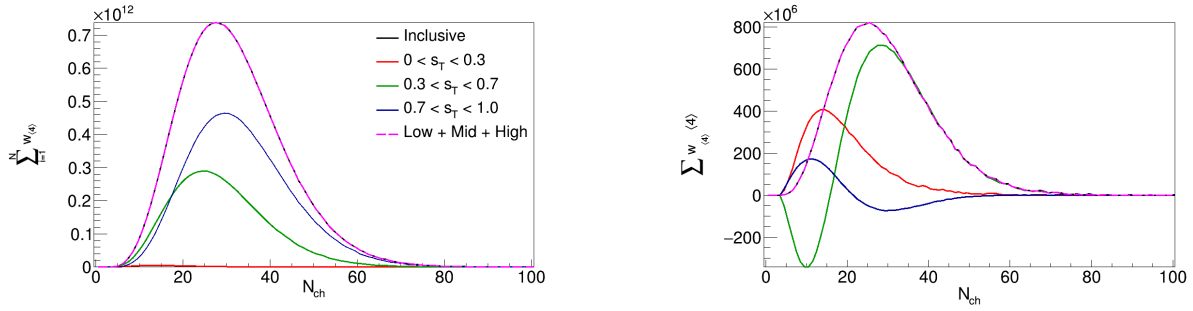
(a) The sum of event weights as a function of multiplicity. The inclusive function can be reconstructed by addition of low, mid and high sphericity.

(b) The sum of weighted correlations as a function of multiplicity. The addition of weighted low, mid and high sphericity again reproduces the now weighted inclusive result.

Figure 19: The weight functions in **(a)** and the non-normalized weighted correlation functions in **(b)**.

$$\langle\langle 4\rangle\rangle \equiv \frac{\left[\sum_{i=1}^{N}\left(W_{\langle 4\rangle}\right)_{i}\langle 4\rangle_{i}\right]_{Low} + \left[\sum_{i=1}^{N}\left(W_{\langle 4\rangle}\right)_{i}\langle 4\rangle_{i}\right]_{Mid} + \left[\sum_{i=1}^{N}\left(W_{\langle 4\rangle}\right)_{i}\langle 4\rangle_{i}\right]_{High}}{\left[\sum_{i=1}^{N}\left(W_{\langle 4\rangle}\right)_{i}\right]_{Low} + \left[\sum_{i=1}^{N}\left(W_{\langle 4\rangle}\right)_{i}\right]_{Mid} + \left[\sum_{i=1}^{N}\left(W_{\langle 4\rangle}\right)_{i}\right]_{High}}. \quad (14)$$

This reconstructed correlation function is shown in figure 18 together with the inclusive result. For $N_{ch} < 60$ the reconstructed and inclusive $\langle\langle 4\rangle\rangle$ do not show any significant differences. However, for higher multiplicities the reconstructed results are not always similar to the inclusive results. The multiplicities at which these dissimilarities occur are equal for all correlation functions and could indicate a statistic uncertainty, but this is not further analysed in this thesis.

5   Conclusion and Outlook

This thesis has presented the results of $c_2\{2\}$, $c_2\{4\}$, $c_2\{6\}$ and $c_2\{8\}$ from both inclusive analysis and explicit analysis of events with low ($0.0 < S_T < 0.3$), mid ($0.3 < S_T < 0.7$) and high ($0.7 < S_T < 1.0$) sphericity. All results are presented as a function of multiplicity and measured in pp-collisions at $\sqrt{s} = 13$TeV.

The multiplicity dependence of the inclusive cumulants is described by a positive sign and does not allow for real valued measurements on v_2, meaning no sign of collective behaviour is observed in these results. The analysis of the three sphericity binned results measured both $c_2\{2\}$ and $c_2\{6\}$ with a positive sign and $c_2\{4\}$ and $c_2\{8\}$ negative. These cumulants allow for real valued measurements on v_2 and already show that the bias created by applying an arbitrary sphericity cut generates signs of collective behaviour without the requirement of a QGP.

The most evident bias is present in the low sphericity analysis, where the event shapes are mostly back-to-back and naturally generate a large v_2, which is measured five times higher in comparison to the maximum value observed in Pb-Pb collisions. The low sphericity events are most dominant in low multiplicity events and their event shape definitely creates bias at low multiplicities. Although the bias here is evident, the data alone does not exclude the existence of a QGP. However, the PYTHIA8 tunes describe qualitatively, the CR-tune sometimes even quantitatively, the same multiplicity dependence as the data. Their consistency shows no QGP contribution is needed to generate the high v_2 values and together with the data they clearly show that it is most likely that v_2 measurements for low multiplicities are not generated by the formation of a QGP, but results solely from the low sphericity event shapes.

The contribution of mid and high sphericity event shapes to the inclusive v_2 measurements are not as straight forward as for low multiplicities. The mid sphericity events do not dominate any multiplicity regime ant their contribution is therefore less defined. The high sphericity events are most dominant for high multiplicities, but their isotropic event shape cannot generate, by definition, high v_2 values. But even now, the CR-tune is still able to describe qualitatively and quantitatively the same multiplicity dependence as the data and continues to support the assumption that even the collective effects observed in mid and high sphericity events do not require the existence of a QGP. However, the hydrodynamic contribution of a QGP to v_2 will be smaller for higher sphericities and therefore needs more detailed analysis extended to higher multiplicities if the existence of a QGP wants to be excluded or proven.

In all analysis the PYTHIA8 tune with colour reconnection performed better in comparison to the regular tune and sometimes even enabled a quantitative description of the data. It thus, can be concluded that colour reconnection improves the PYTHIA8 performance and the observations in this thesis support the argument that colour reconnection could be involved by the collective effects observed in small systems. However, even with colour reconnection the model slightly underestimates most plateaus reached with v_2. A more detailed study on these differences is needed to conclude where they originate. This could be achieved by the data analysis of upcoming LHC runs that will provide more statistics and can extend the study to higher multiplicities.

As a final point, the reconstruction of inclusive sphericity can only be done at the level of correlation functions and has shown some specific multiplicity dependent dissimilarities. This could be caused by a systematic uncertainty in the inclusive analysis or in the sphericity binned results and could be something to consider in further analysis.

Acknowledgements

In this final part of my thesis, I would like to thank my supervisor Panos Christakoglou. During my research project, he has provided me with useful feedback and always put great effort in answering my questions. I appreciate the time he took to discuss my progress on a weekly basis, especially since we were unable to meet in person due to the corona virus. That is why I also want to thank Lars, who provided me a with a place to study in times it was hard to stay focussed at home.

References

[1] Y. Aoki, G. Endrdi, Z. Fodor, S. D. Katz, and K. K. Szab. The order of the quantum chromodynamics transition predicted by the standard model of particle physics. *Nature*, 443(7112):675678, Oct 2006.

[2] R. K. Ellis, W. J. Stirling, and B. R. Webber. Fundamentals of QCD. page 121, 1996.

[3] Peter Braun-Munzinger and Johanna Stachel. The quest for the quark-gluon plasma. *Nature*, 448:302–309, 2007.

[4] Panagiota Foka and. Overview of results from ALICE at the CERN LHC. *Journal of Physics: Conference Series*, 455:012004, aug 2013.

[5] Ante Bilandzic, Raimond Snellings, and Sergei Voloshin. Flow analysis with cumulants: Direct calculations. *Physical Review C*, 83(4), Apr 2011.

[6] Jamie Dunlop. Strange brew: Probing the flow of (strange) quarks with identified particles. *RHIC News*, 2007 Edition, Mar 2007.

[7] Matthew Luzum and Jean-Yves Ollitrault. Extracting the shear viscosity of the quark-gluon plasma from flow in ultra-central heavy-ion collisions. *Nucl. Phys. A*, 904-905:377c–380c, 2013.

[8] V. Khachatryan, A.M. Sirunyan, A. Tumasyan, W. Adam, E. Asilar, T. Bergauer, J. Brandstetter, E. Brondolin, M. Dragicevic, J. Er, and et al. Measurement of long-range near-side two-particle angular correlations in pp collisions at s=13tev. *Physical Review Letters*, 116(17), Apr 2016.

[9] S. Acharya, D. Adamov, S.P. Adhya, A. Adler, J. Adolfsson, M.M. Aggarwal, G. Aglieri Rinella, M. Agnello, N. Agrawal, Z. Ahammed, and et al. Investigations of Anisotropic Flow Using Multiparticle Azimuthal Correlations in pp, p-Pb, Xe-Xe, and Pb-Pb Collisions at the LHC. *Physical Review Letters*, 123(14), Oct 2019.

[10] S. Voloshin and Y. Zhang. Flow study in relativistic nuclear collisions by Fourier expansion of azimuthal particle distributions. *Zeitschrift fr Physik C particles and Fields*, 70(4):665671, May 1996.

[11] Nicolas Borghini, Phuong Mai Dinh, and Jean-Yves Ollitrault. New method for measuring azimuthal distributions in nucleus-nucleus collisions. *Physical Review C*, 63(5), Apr 2001.

[12] Raimond Snellings. Elliptic flow: a brief review. *New Journal of Physics*, 13(5):055008, May 2011.

[13] Nicolas Borghini, Phuong Mai Dinh, and Jean-Yves Ollitrault. Is the analysis of flow at the CERN Super Proton Synchrotron reliable? *Physical Review C*, 62(3), Aug 2000.

[14] S. Acharya, F. T.-. Acosta, D. Adamov, J. Adolfsson, M. M. Aggarwal, G. Aglieri Rinella, M. Agnello, N. Agrawal, Z. Ahammed, and et al. Energy dependence and fluctuations of anisotropic flow in Pb-Pb collisions at $\sqrt{s_{\mathrm{NN}}} = 5.02$ and 2.76 tev. *Journal of High Energy Physics*, 2018(7), Jul 2018.

[15] Arvind Khuntia, Sushanta Tripathy, Ashish Bisht, and Raghunath Sahoo. Event Shape Engineering and Multiplicity dependent Study of Identified Particle Production in proton+proton Collisions at $\sqrt{s}$= 13 tev using PYTHIA, 2018.

[16] ALICE Collaboration. Performance of the ALICE experiment at the CERN LHC. *International Journal of Modern Physics A*, 29(24):1430044, Sep 2014.

[17] The Collaboration, Kjeld Aamodt, Arian Abrahantes, Ricardo Achenbach, S Acounis, Dagmar Adamova, C Adler, M Aggarwal, F Agnese, Gianluca Aglieri Rinella, Zubayer Ahammed, A Ahmad, Nora Ahmad, Shakeel Ahmad, A Akindinov, P Akishin, D Aleksandrov, Borri Alessandro, Romulo Alfaro, and M Zuffa. The alice experiment at the CERN LHC. *Journal of Instrumentation*, 3:S08002, 08 2008.

[18] S. Beol. The ALICE Inner Tracking System: Performance with Proton and Lead Beams. *Physics Procedia*, 37:1062 – 1069, 2012. Proceedings of the 2nd International Conference on Technology and Instrumentation in Particle Physics (TIPP 2011).

[19] P. Kuijer. The inner tracking system of the Alice experiment. *Nuclear Instruments and Methods in Physics Research Section A: Accelerators, Spectrometers, Detectors and Associated Equipment*, 530(1):28 – 32, 2004. Proceedings of the 6th International Conference on Large Scale Applications and Radiation Hardness of Semiconductor Detectors.

[20] O. Schäfer. Working principle of a TPC.

[21] J. Alme, Y. Andres, H. Appelshuser, S. Bablok, N. Bialas, R. Bolgen, U. Bonnes, R. Bramm, P. Braun-Munzinger, R. Campagnolo, and et al. The ALICE TPC, a large 3-dimensional tracking device with fast readout for ultra-high multiplicity events. *Nuclear Instruments and Methods in Physics Research Section A: Accelerators, Spectrometers, Detectors and Associated Equipment*, 622(1):316367, Oct 2010.

[22] The ALICE collaboration. Performance of the ALICE VZERO system. *Journal of Instrumentation*, 8(10):P10016P10016, Oct 2013.

[23] J. Conrad, J.G. Contreras, and C.E. Jorgensen. Minimum bias triggers in proton-proton collisions with VZERO and pixel detectors. 2005.

[24] Data Preparation Group. ALICE data flow. Powerpoint Presentation, Nov 2017.

[25] Lara De Nardo. On the Propagation of Statistical Errors, Mar 2002.

[26] Torbjrn Sjstrand, Stephen Mrenna, and Peter Skands. A brief introduction to PYTHIA 8.1. *Computer Physics Communications*, 178(11):852867, Jun 2008.

[27] I A Maldonado-Cervantes, E Cuautle, Guy Paic, A Ortiz Velasquez, and Peter Christiansen. Color reconnection and flow-like patterns in pp collisions. *Journal of Physics: Conference Series*, 509:012064, may 2014.

[28] Richard Corke and Torbjrn Sjstrand. Interleaved parton showers and tuning prospects. *Journal of High Energy Physics*, 2011(3), Mar 2011.
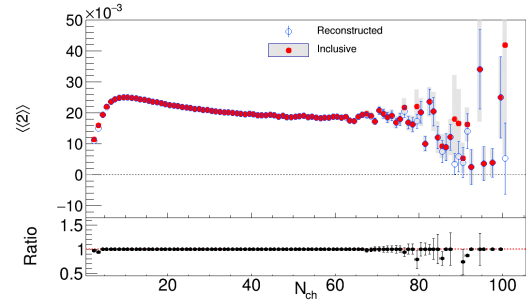
A   Appendix
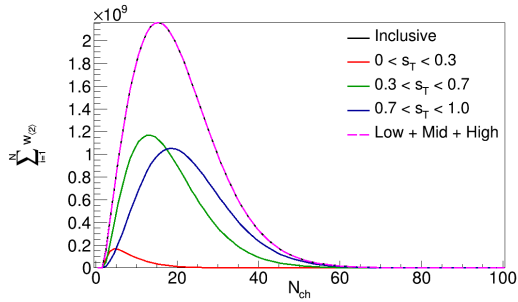
A.1   Reconstruction of Inclusive Sphericity

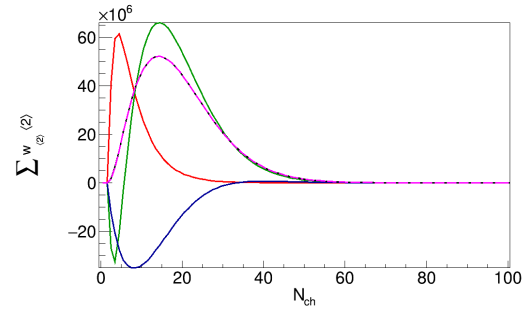### A.1.1 $\langle\langle 2 \rangle\rangle$
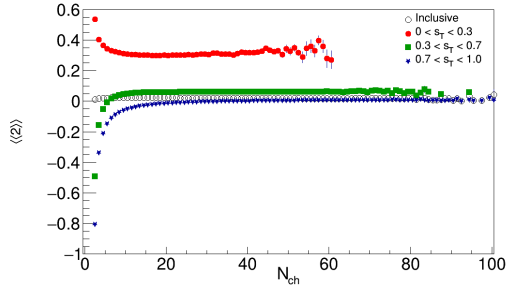
(a) The multiplicity dependence of $\langle\langle 2 \rangle\rangle$ for the inclusive analysis together with the results from low, mid and high sphericity analysis.
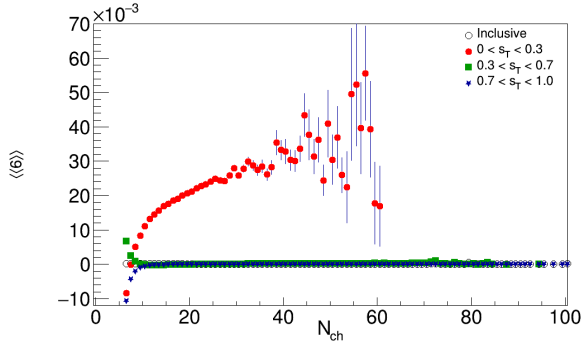

(b) The multiplicity dependence of both $\langle\langle 2 \rangle\rangle$ from inclusive analysis and reconstructed from the mid, low and high sphericity analysis.
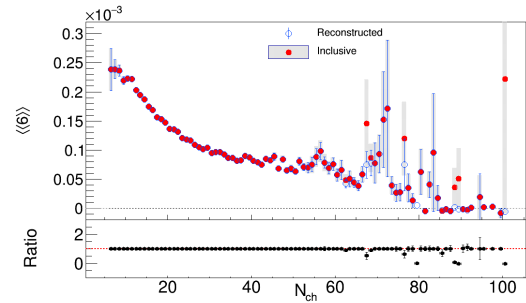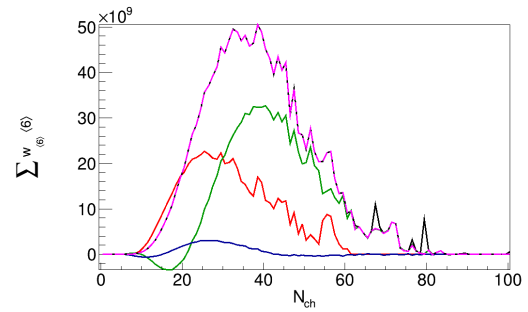

(c) The sum of event weights as a function of multiplicity. The inclusive function can be reconstructed by addition of low, mid and high sphericity.

(d) The sum of weighted correlations as a function of multiplicity. The addition of weighted low, mid and high sphericity again reproduces the now weighted inclusive result.

A.1.2 $\langle\langle 6 \rangle\rangle$

(a) The multiplicity dependence of $\langle\langle 6 \rangle\rangle$ for the inclusive analysis together with the results from low, mid and high sphericity analysis.
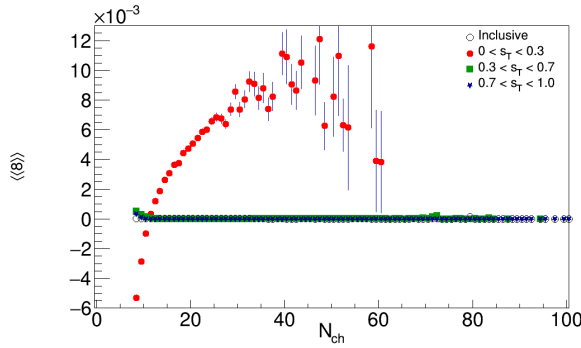

(b) The multiplicity dependence of both $\langle\langle 6 \rangle\rangle$ from inclusive analysis and reconstructed from the mid, low and high sphericity analysis.
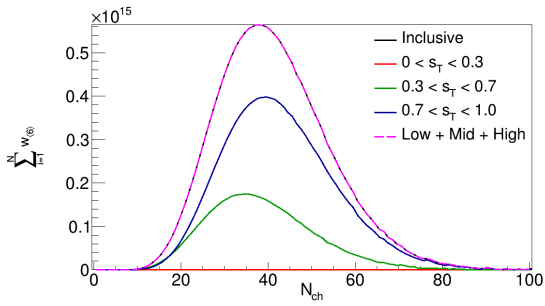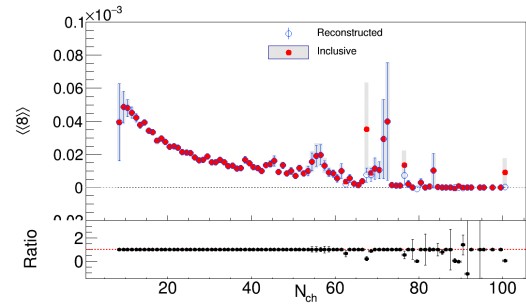

(c) The sum of event weights as a function of multiplicity. The inclusive function can be reconstructed by addition of low, mid and high sphericity.
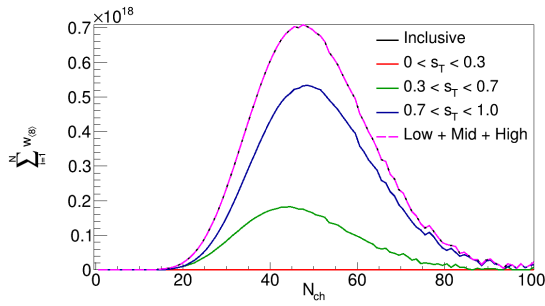

(d) The sum of weighted correlations as a function of multiplicity. The addition of weighted low, mid and high sphericity again reproduces the now weighted inclusive result.

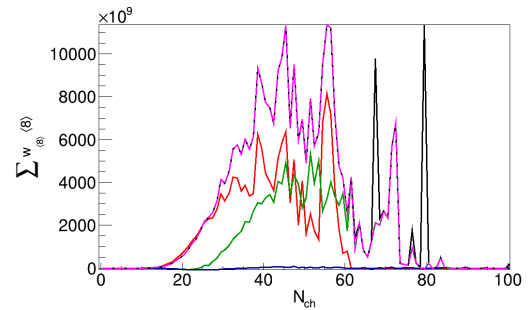### A.1.3 $\langle\langle 8 \rangle\rangle$

(a) The multiplicity dependence of $\langle\langle 8 \rangle\rangle$ for the inclusive analysis together with the results from low, mid and high sphericity analysis.

(b) The multiplicity dependence of both $\langle\langle 8 \rangle\rangle$ from inclusive analysis and reconstructed from the mid,low and high sphericity analysis.

(c) The sum of event weights as a function of multiplicity. The inclusive function can be reconstructed by addition of low, mid and high sphericity.

(d) The sum of weighted correlations as a function of multiplicity. The addition of weighted low, mid and high sphericity again reproduces the now weighted inclusive result.